

1 Elastic anisotropies of deformed upper crustal rocks in the Alps

2
3 Ruth Keppler (1), Roman Vasin (2), Michael Stipp, (3), Tomáš Lokajíček (4), Matej Petružálek (4), Nikolaus
4 Froitzheim (1)

5
6 Corresponding author: Ruth Keppler (rkep@uni-bonn.de)

7
8 ¹ Institute for Geosciences, University of Bonn, Poppelsdorfer Schloss, D-53115 Bonn, Germany

9 ² Frank Laboratory of Neutron Physics, Joint Institute for Nuclear Research, Joliot-Curie 6, 141980 Dubna,
10 Russia

11 ³ Institute for Geosciences and Geography, Von-Seckendorff-Platz 3, D-06120 Halle (Saale), Germany

12 ⁴ Institute of Geology of the Czech Academy of Sciences, Rozvojova 269, 16000 Prague 6, Czech Republic

13
14
15 ABSTRACT

16
17 The ~~upper~~ crust within collisional orogens is very heterogeneous both in composition and grade of
18 deformation, leading to ~~very highly~~ variable physical properties at small scales. This ~~causes yields~~
19 difficulties for seismic investigations of tectonic structures at depth since ~~the diverse and partially strong~~
20 ~~upper crustal anisotropy might overprint the signal of deeper anisotropic structures in the mantle local~~
21 ~~changes in elastic anisotropy cannot be detected~~. In this study, we ~~characterize the range of show~~ elastic
22 anisotropies ~~of the range of typical lithologies within~~ deformed ~~upper~~ crustal rocks in the Alps.
23 Furthermore, we ~~aim to~~ model average elastic anisotropies ~~offer~~ these rocks and their changes with
24 increasing depth due to the closure of microcracks. ~~We therefore sampled~~ ~~For that pre-Alpine upper crustal~~
25 rocks ~~of in~~ the Adula Nappe ~~in of~~ the central Alps, which ~~originates from pre-Alpine upper crust and was~~
26 ~~were intensely deformed is typical for upper crust in during the Alpine orogeny, were sampled collisional~~
27 ~~orogens~~. The two major rock types found are orthogneisses and paragneisses, however, small lenses of
28 metabasites and marbles also occur. Crystallographic preferred orientations (CPOs) and volume fractions
29 of minerals in the samples were measured using time-of-flight neutron diffraction. Combined with single
30 crystal elastic anisotropies these were used to model seismic properties of the rocks. The sample set shows
31 a wide range of different seismic velocity patterns even within the same lithology, due to the
32 ~~microstructural~~ heterogeneity of ~~the~~ deformed ~~upper~~ crustal rocks. To approximate an average for these
33 ~~upper~~ crustal units, we picked common CPO types of rock forming minerals within ~~the~~ gneiss samples,
34 ~~which~~ representing the most common lithology. These data were used to determine an average elastic
35 anisotropy of a typical ~~upper~~ crustal rock within the Alps. Average mineral volume percentages within the
36 gneiss samples were used for the calculation. In addition, ultrasonic ~~anisotropy~~ measurements ~~of elastic~~
37 ~~anisotropies~~ of the samples at increasing ~~confining~~ pressures were performed. These measurements, as
38 well as the microcrack patterns ~~determined in thin sections of the samples~~ were used to model the closure
39 of microcracks in the average sample at increasing depth. ~~At ~740 MPa m~~ Microcracks are ~~assumed to be~~
40 closed ~~at approximately 740 MPa~~ yielding average elastic anisotropies of 4% for the average gneiss. This
41 value is an approximation, which can be ~~helpful used~~ for seismic models at a lithospheric scale. At a crustal
42 or smaller scale, however, ~~it is an oversimplification and~~ local ~~variations in~~ lithology ~~and~~ ~~as well as~~

43 deformational changes shown as displayed by the range of elastic anisotropies within the sample set have
44 need to be considered. In addition, larger scale structural anisotropies such as layering, intrusions, as well
45 as brittle faults have to be included in any crustal scale seismic model.

49 1. Introduction

51 Geophysical studies of the Earth's crust and mantle of the Earth are constantly continuously improving
52 and allowing for more and more detailed structural investigations of structures due to higher resolutions
53 at increasingly higher-greater depth are possible due to higher resolutions. High-resolution geophysical
54 imaging of 3D structures is currently taking place carried out within the AlpArray initiative using a high-end
55 seismological array in the Alpine orogenorogeny (Hetényi et al., 2018). For this as well as other similar
56 projects around the world there is a demand for precise input parameters and knowledge of the physical
57 properties of the rocks at depth is required. Especially elastic anisotropy data is-are of importance, since
58 they it reflects the plastic deformation of rocks shearing at depth. Rock elastic anisotropy of at mantle
59 rocks depth is mainly-in large parts caused by the crystallographic preferred orientation (CPO) of the
60 constituent mineral phases (Silver, 1996; Montagner and Guillot, 2003). Besides CPO other rock fabrics
61 such as compositional layering, grain and aggregate size and shape, grain boundaries and shape preferred
62 orientation can bear an influence. At shallower-lower depth microcracks additionally influence-modify
63 elastic properties by both lowering the seismic velocity and increasing the elastic anisotropy
64 properties anisotropy in deformed rocks. The elastic rock properties can be either be gained by
65 measurements using ultrasound, including experiments at high pressures and temperatures (e.g.,
66 Christensen, 1965; Babuška, 1968; Christensen, 1979; Christensen and Mooney, 1995; Kern and Wenk,
67 1990; Pros et al., 2003), or modeled using the CPO data of the constituent minerals and their
68 corresponding single crystal elastic anisotropies (e.g., Mainprice and Humbert, 1994; Bascou et al., 2001;
69 Cholach and Schmitt, 2006; Llana-Fúnez and Brown, 2012; Almqvist and Mainprice, 2017; Puelles et al.,
70 2018). Many works combine these two approaches to highlight the effect of individual minerals on elastic
71 wave velocities in bulk rock, or to infer the influence of pores and fractures (e.g., Ji and Salisbury, 1993; Ji
72 et al., 1993; Barruol and Kern, 1996; Mauler et al., 2000; Ji et al., 2003; Ivankina et al., 2005; Kitamura,
73 2006; Kern et al., 2008; Ábalos et al., 2010; Lokajicek et al., 2014; Keppler et al., 2015; Vasin et al., 2017;
74 Ullemeyer et al., 2018). Elastic anisotropy data of rocks can be either be gained obtained by measurements
75 in high-pressure vessels using ultrasound or modeled using the CPO data of the constituent minerals and
76 their corresponding single crystal elastic anisotropies (e.g., Christensen 1965; Babuška, 1968; Kern and
77 Wenk, 1990; Ji et al. 1993; Mainprice and Humbert, 1994; Christensen et al., 1995; Barruol and Kern, 1996;
78 Mauler et al., 2000; Bascou et al., 2001; Ji et al., 2003; Pros et al., 2003; Ivankina et al., 2005; Kitamura,
79 2006; Kern et al., 2008; Ábalos et al., 2011; Lana-Fúnez and Brown, 2012; Lokajicek et al., 2014; Keppler et
80 al., 2015; Almqvist and Mainprice, 2017; Vasin et al., 2017; Ullemeyer et al., 2018), or modeled using the
81 CPO data of the constituent minerals and their corresponding single crystal elastic anisotropies (e.g.
82 Mainprice and Humbert, 1994; Barruol and Kern, 1996; Mauler et al., 2000; Bascou et al., 2001; Ivankina
83 et al., 2005; Kitamura, 2006; Kern et al., 2008; Abalos et al., 2010; Llana-Fúnez and Brown, 2012; Keppler
84 et al., 2015; Almqvist and Mainprice, 2017). During in experimental investigations measurements,

85 ~~microcracks in rock samples are not completely closed~~, despite pressure vessels operating at up to
86 ~~hundreds of 600 MPa during measurements~~, ~~microcracks in rock samples are not completely closed~~ (e.g.
87 Christensen, 1974; Kern et al., 2008; Matthies, 2012; Vasin et al., 2017), ~~which~~ ~~That~~ is why ~~the~~ resulting
88 data are only comparable to elastic anisotropies ~~within of~~ ~~normal~~-crustal depth, whereas the modeled
89 anisotropies yield results for a crack free medium at higher depths (e.g., within thickened crust or at mantle
90 depth).

91 ~~The problem~~ ~~When~~ using elastic anisotropy data of natural rocks as input parameters for seismic
92 investigation ~~is the difference in scale~~. ~~There~~ ~~the~~ ~~is~~ a gap between the km-scale of detectable units in
93 seismic imaging at depth and the centimeter-sized rock samples taken from outcrops ~~of several~~ ~~in~~ meter
94 ~~scales must be considered~~ ~~in the field~~. This ~~is not less of an issue~~ ~~difference in scale is less problematic for~~
95 ~~in~~ the relatively homogenous mantle ~~rocks~~ with a fairly simple mineralogy (e.g. Mainprice et al., 2000;
96 Karato et al., 2008), but even in the mantle ~~compositional heterogeneities leading to elastic anisotropies~~
97 ~~have been observed~~ (Faccenda et al., 2019). Crustal rocks, ~~however~~, are not only polymineralic but ~~the~~
98 lithologies ~~are~~ ~~variable~~ ~~significantly vary in composition~~. Additionally, deformation is also ~~very~~
99 heterogeneous within the crust. Especially subduction zones and collisional orogens show a complex
100 deformational history (e.g., Schmid et al., 2004; Simancas et al., 2005; Zhang et al., 2012). This ~~leads~~
101 ~~to results in~~ a large variety of ~~different~~-CPO patterns throughout a ~~km~~-kilometer scale geological unit
102 (Schmidtke et al. ~~submitted to same issue~~2021). Averaging the calculated or measured elastic anisotropies
103 may lead to the ~~prediction~~ ~~assumption~~ of an unrealistically isotropic medium, for these ~~more~~ strongly
104 deformed parts of the crust. ~~There are only a few studies, which aim to close the gap between the elastic~~
105 ~~anisotropy gained from hand samples-sized volumes and the one measured in seismic experiments of the~~
106 ~~crust and mantle~~ (Okaya et al., 2019; Zertani et al., 2020). Okaya et al. (2019) investigated the influence of
107 ~~local structures such as folds, domes or shear zones on the bulk anisotropic properties of larger units.~~
108 ~~Using tensor algebra they separate these local structures from an already overall anisotropic rock, which~~
109 ~~allows to quantify the role of macroscale structures.~~ Zertani et al. (2020) used the finite element method
110 ~~to model petrophysical properties of meter to kilometer scale eclogite units, which could allow to visualize~~
111 ~~structures in active subduction and collision zones by geophysical methods.~~

112 ~~It is therefore essential to~~ ~~in the present work, we~~ classify the crust according to its composition and grade
113 of deformation ~~in order~~ to define larger units which can be summarized. Since only deformed parts of the
114 crust exhibit elastic anisotropy, this study is focused on the Adula Nappe of the Central Alps. ~~Originating~~
115 ~~from pre-Alpine upper crust mainly made up of granitoids and Mesozoic sediments, the Adula Nappe,~~
116 ~~which is representative for upper crustal rocks~~ ~~was intensely~~ deformed during the Alpine Orogeny. CPO as
117 well as volume percentages of all mineral phases from a large set of samples of this unit were determined.
118 Subsequently, elastic anisotropies of the samples were calculated. These show a wide range of seismic
119 properties of deformed ~~upper~~ crustal rocks in the Alps. Most of the samples are gneisses, which represent
120 the most common rock type in the Adula Nappe. Based on the characteristic CPO types, average CPO
121 strengths and average volume percentages of the relevant mineral phases, we calculated the elastic
122 anisotropy of an “average rock”, which represents an average anisotropy for deformed ~~upper~~ crustal rocks
123 in collisional orogens. The two major lithologies are orthogneisses and paragneisses, which is why the
124 “average rock” has typical gneiss CPO and composition. ~~Furthermore, at shallow depth~~ ~~Because of the~~
125 ~~importance of~~ microcracks ~~at shallow depth~~ ~~within the rocks are an important factor~~. Therefore, we used
126 data from ultrasonic measurements as well as thin section analysis to determine typical crack patterns in

127 the samples. From these the influence of microcracks on elastic properties was quantified, as well as the
128 changes in elastic anisotropy with increasing depth up to the point where all microcracks are presumably
129 closed.

130 This is, of course, a simplification of the very heterogeneous ~~upper~~ crust of the Alps, as already shown by
131 the variability of elastic anisotropy of the individual samples from the Adula Nappe. Yet, such an average
132 rock can be used for lithospheric and upper mantle scale seismic models, in which the crust is implemented
133 as a single unit with an average anisotropy. ~~In At crustal scale models~~ the heterogeneity of different rocks
134 caused by variable composition as well as variable deformation have to be considered. While it is difficult
135 to present a universal average anisotropy for the very heterogeneous crust within collisional orogens, this
136 contribution ~~represents a first approximation to close~~ aims to bridge the scale gap between elastic
137 anisotropy data of rock samples and the kilometer scale structures measured in seismic investigations ~~at~~
138 greater depth by considering heterogeneities in composition and structure as well as the reduction of crack
139 porosity with increasing depth.

140

141

142 2. Elastic anisotropies within the Alpine orogen

143

144 The Alpine ~~o~~rogen exhibits a mountain-belt-parallel seismic anisotropy (e.g., Silver, 1996; Smith and
145 Ekström, 1999; [Bokelmann et al., 2013](#); [Petrescu et al., 2020](#)), which is not completely understood. In the
146 Western Alps this anisotropy was illustrated by teleseismic shear wave splitting and interpreted as a result
147 of asthenospheric flow beneath the lithospheric slab, although a further influence by lithospheric
148 anisotropy due to Alpine deformation could not be excluded (Barruol et al., 2004; 2011). Fry et al. (2010),
149 on the other hand, determined seismic anisotropies within the Alps by passive seismic imaging using
150 Rayleigh wave phase velocities. Their results suggest two distinct vertically distributed layers of anisotropy
151 – an orogen-parallel fast direction down to 30 km and an orogen-perpendicular one between 30 and 70
152 km depth - with differ~~ingent~~ geodynamic origins. The authors interpret the orogen-parallel anisotropy as
153 a consequence of the CPO of crustal minerals (e.g. amphibole and biotite) in response to compression and
154 consider the deeper, orogen-perpendicular anisotropy to result from bending and flow of the European
155 lithospheric mantle. This two-layer anisotropy was also detected from SKS-splitting in the transition to the
156 Eastern Alps. The two layers were interpreted as asthenospheric flow above a detached lithospheric slab
157 fragment with mountain chain parallel CPO (Qorbani et al., 2015; Link and Rumpker, 2021).

158 The Alps have a fairly complicated tectonic history with two major collisional events involving several
159 oceans and microcontinents. While the cretaceous Eoalpine event only involved the Eastern Alps, the
160 Tertiary deformation event incorporated the complete Alpine orogen. Here, we concentrate on one
161 specific profile. T

162 he deep structure of the Western and Central Alps ~~that is~~ mainly ~~the~~ result ~~of~~ ~~from~~
subduction and collision processes during the Paleogene and Neogene tectonics when the Penninic ocean
163 basins were subducted and Adria, Iberia, and other continental fragments collided with Europe. We
164 consider a simplified version of the NFP-20 EAST&EGT profile (Fig. 1A; Schmid and Kissling, 2000) ~~and~~ ~~We~~
165 exclude nappe structures in the shallowest part of the profile, like the Helvetic nappes. This results in a
166 profile including the following upper crustal units: the Aar and Gotthard massifs representing weakly
167 deformed European basement; the Lucomagno, Simano and Adula nappes of deformed European

168 basement and Mesozoic cover; and relatively undeformed Apulian upper crust. To simplify, we therefore
 169 subdivide the profile into

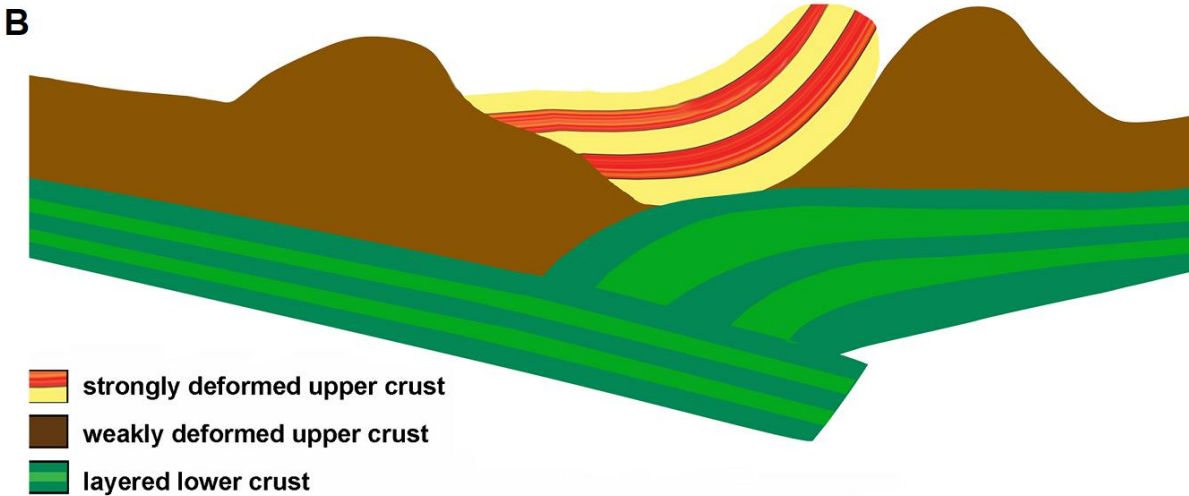
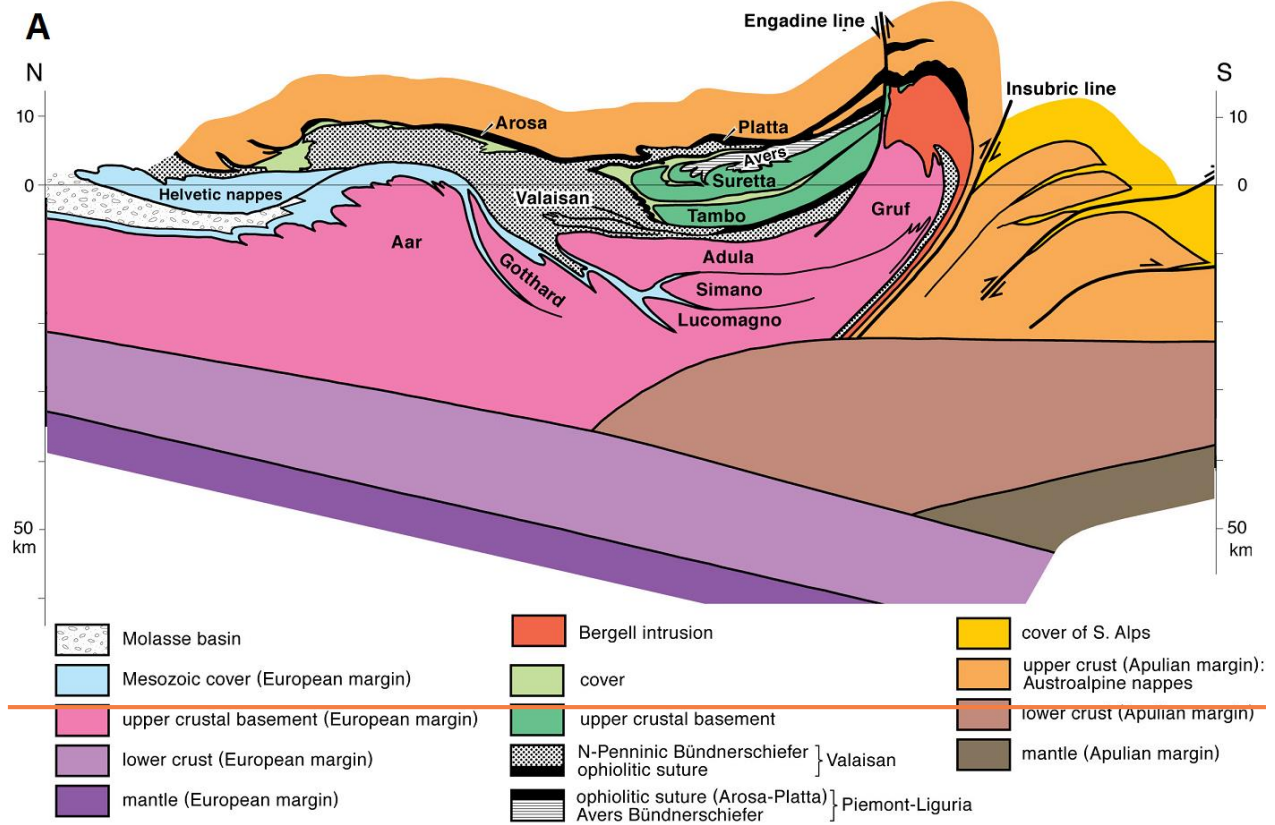
170

171 (1) weakly deformed and isotropic upper crust

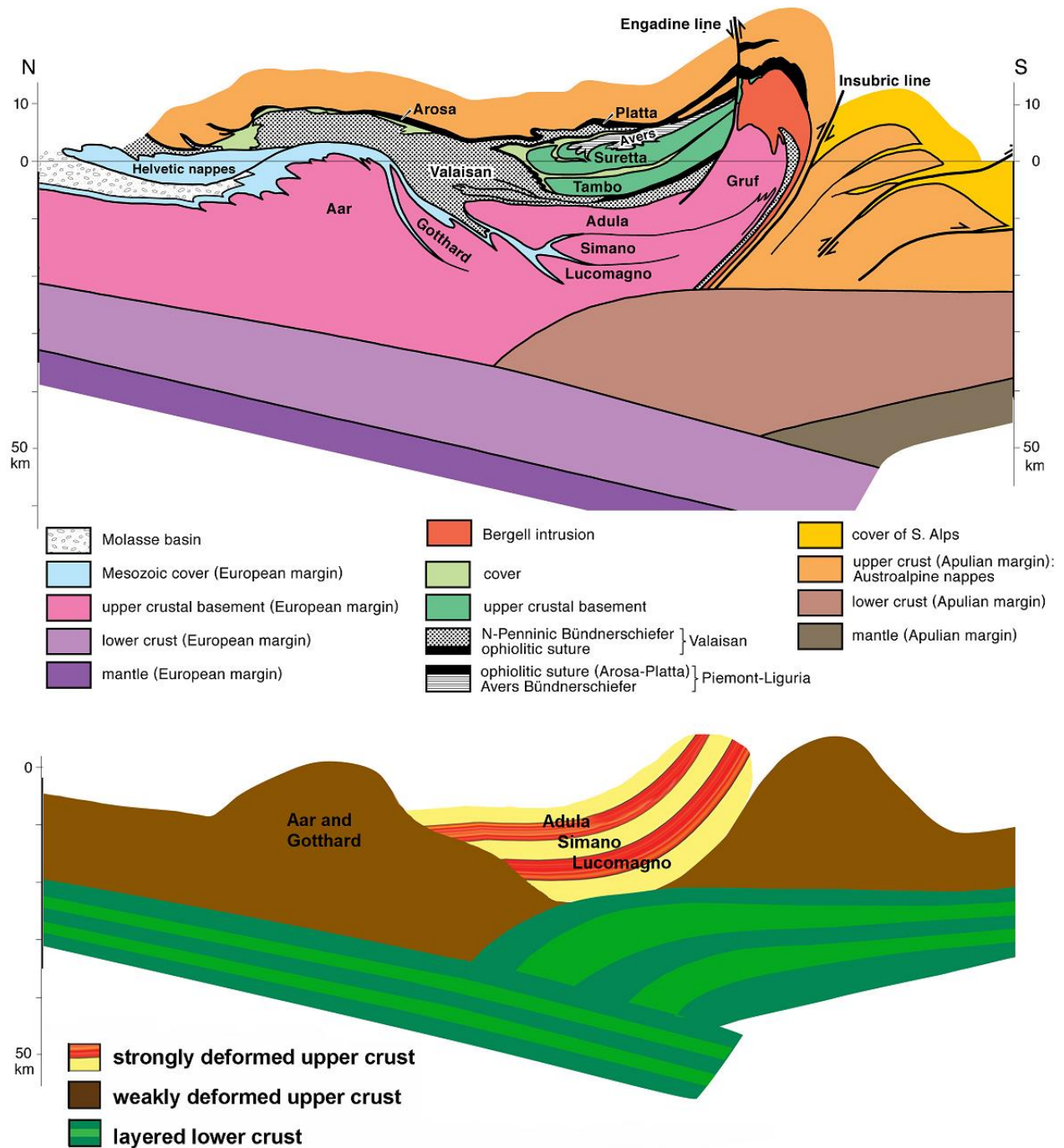
172

173 (2) strongly deformed anisotropic upper crust mostly comprising gneiss (Fig. 1B).

174



175



176
 177 Figure 1: (A) North-south tectonic profile through the central Alps showing all major units (NFP-20
 178 EAST&EGT; Schmid and Kissling, 2000) (B) strongly simplified profile through the same units,
 179 representing consisting of the predominant type of rock units and neglecting the sedimentary cover and
 180 ophiolite units

181
 182 2.1. Weakly deformed Alpine upper crust
 183

184 In this study, both the crystalline massifs in the northern part of the central Alps and the Adriatic basement
185 in the Southern Alps are assumed to show weak or no elastic anisotropy.

186 The Aar and Gotthard massifs contain large Variscan granitoid bodies which intruded into a pre-Variscan
187 basement. These units ~~have—were~~ only weakly ~~been~~ overprinted by Alpine metamorphism and
188 deformation (e.g., Abrecht, 1994; Schaltegger, 1994; Oliot et al., 2010). However, some greenschist to
189 amphibolite facies shear zones have been documented, which have to be considered for any large scale
190 model (Challandes et al., 2008; Goncalves et al., 2012; Wehrens et al., 2017). In addition structures related
191 to the evolution of Gondwana in the pre-Variscan basement, in which the granitoids intruded also have to
192 be regarded (e.g. von Raumer et al., 2013). Furthermore, Jurassic rifting structures are present in parts of
193 the Penninic nappes (e.g. Froitzheim and Manatschal, 1996). Even though these structures are mostly
194 related to brittle deformation, they might cause local seismic anisotropies.

195 In the Southern Alps, metamorphic grade during deformation was generally low. Deformation in the
196 basement is limited to large scale thrust ~~faultsing~~ during Alpine tectonics (e.g., Laubscher 1985). For
197 simplification, we are assuming an elastically isotropic medium for both the ~~Variscan granitoids~~ Aar and
198 Gotthard massifs of the European margin and the ~~S~~outhern Alps due to the lack of pervasive CPO forming
199 deformation. ~~One needs to bear in mind h~~However, ~~that~~ local ductile shear zones as well as large brittle
200 faults also have an influence on the overall elastic anisotropy (e.g. Almqvist et al., 2013).

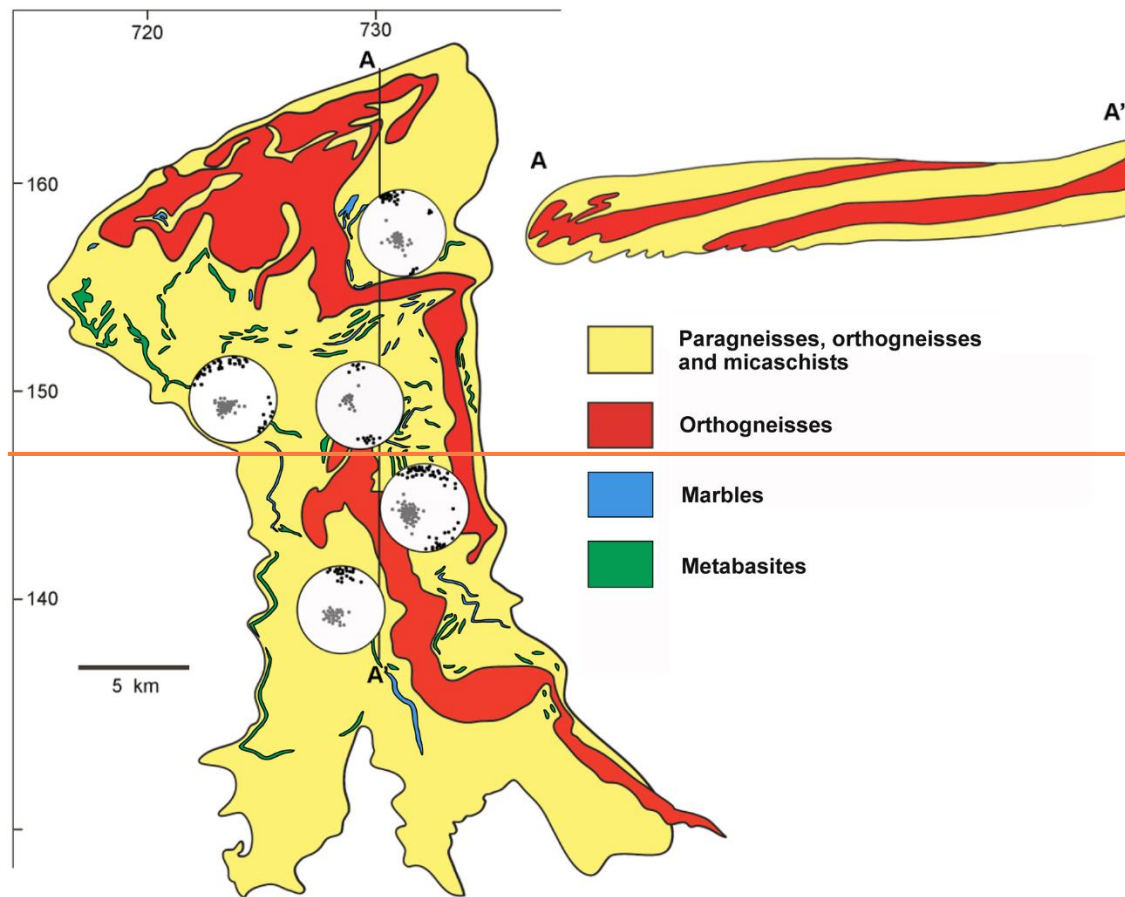
201 Of course one needs to bear in mind that considering the crystalline massifs in the northern part of the
202 central Alps and the Adriatic basement as isotropic is a strong simplification of complex structures with a
203 long deformational history. In addition to brittle deformation structures, lithological layering as well as
204 intrusions may be further factors influencing the overall anisotropy of crustal scale seismic models.

205

206 2.2. Strongly deformed Alpine upper crust

207

208 As ~~suggested—indicated~~ by numerous geological field studies as well as strong reflectors in the original NFP-
209 20-east seismic profile (Pfiffner et al., 1988), ~~as well as numerous geological field studies~~, the crustal units
210 in the ~~main~~central part (concerning their position in the N-S running profile) of the central Alps have been
211 strongly deformed during subduction and subsequent continental collision (Fig. 1B).
212

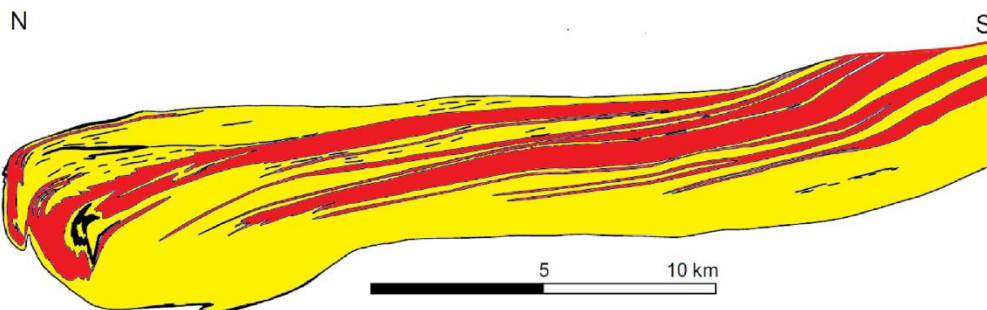
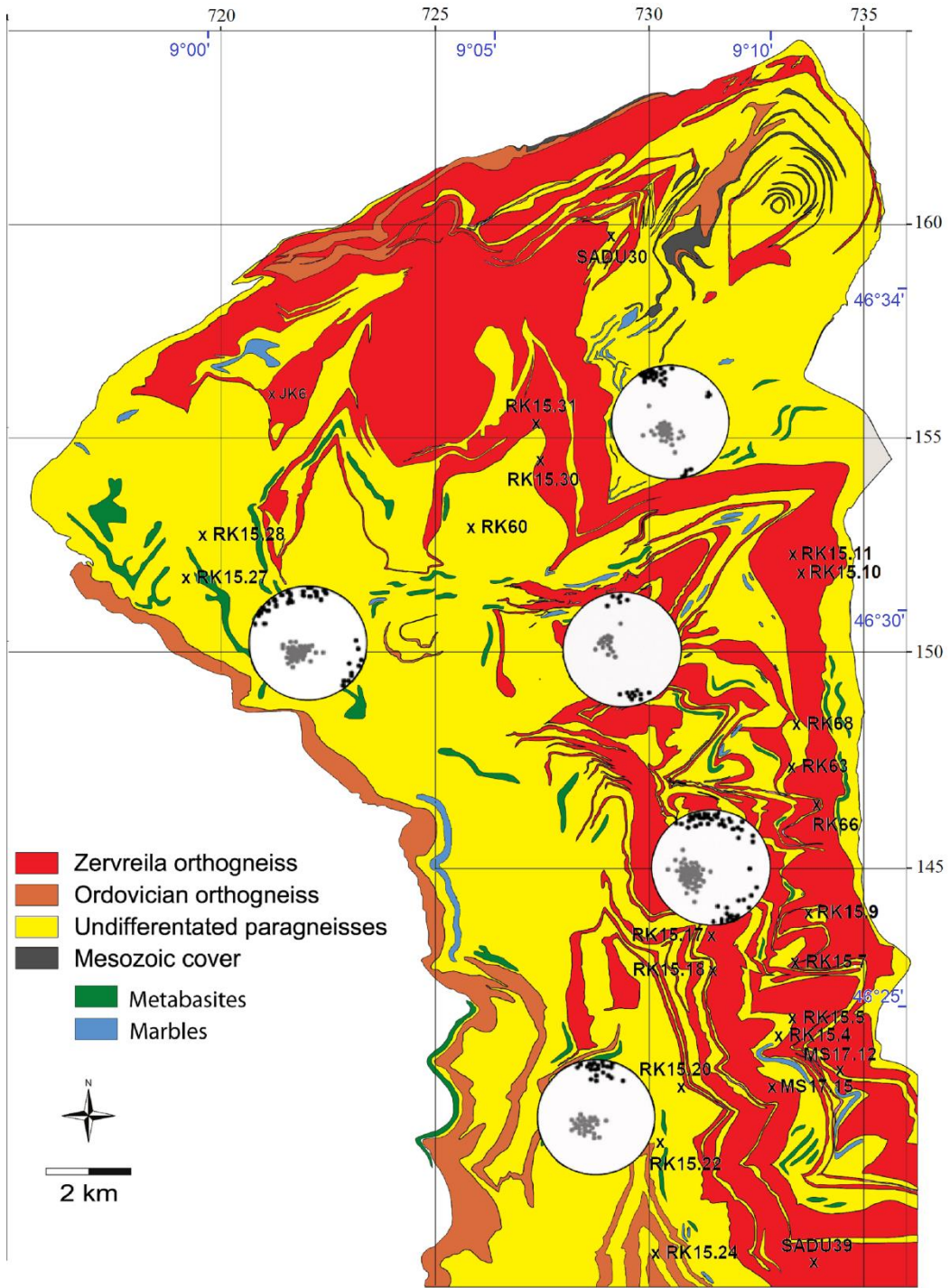


213
 214 ~~Figure 2: Simplified tectonic map and north-south profile of the Adula Nappe in the Swiss coordinate~~
 215 ~~system (after Nagel, 2008). Grey and black dots indicate poles of main foliation and stretching lineation,~~
 216 ~~respectively, in the central Adula Nappe.~~

217
 218 The Adula Nappe together with the Simano and Lucomagno nappes constitutes the Lepontine dome,
 219 which mostly consists of Alpine nappes including Variscan basement and its Mesozoic cover (e.g. Engi et
 220 al., 1995; Nagel et al., 2002). In this study, the Adula Nappe is taken as an example for the strongly
 221 deformed parts of the Alps, ~~it~~ representing a relatively coherent unit with stratigraphic basement-cover
 222 contacts. ~~It comprises orthogneisses from Cambrian, Ordovician, and Permian protoliths (Cavargna-Sani~~
 223 ~~et al. 2014), paragneisses with metabasic lenses, and some layers of marble (Fig. 2).~~ It was originally part of
 224 the distal European continental margin and entered a south-dipping subduction zone in which the Valais
 225 (North Peninnic) Ocean had been consumed. The unit shows peak conditions of 12–17 kbar/500–600 C° in
 226 the north and 30 kbar/800–850 C° in the south (e.g. Heinrich, 1986; Löw, 1987; Meyre et al., 1997; Nagel
 227 et al. 2002; Dale and Holland, 2003). ~~Lu–Hf garnet ages revealed an Eocene age for UHP metamorphism~~
 228 ~~(35–38 Ma; Sandmann et al., 2014) It mainly comprises orthogneisses and paragneisses with interlayers of~~
 229 ~~schists, quartzites, marbles and metabasic lenses (Fig. 2).~~ All lithologies found in the nappe were sampled,
 230 however most samples are orthogneisses and paragneisses, since these lithologies make up the largest
 231 part of the nappe and other lithologies might be too small scale to be detected in seismic imaging.
 232 ~~However, since these layers of different lithology could be significant for the overall anisotropy two~~
 233 ~~metabasalts as well as a marble sample have been included in the sample set.~~

234 From peak conditions to its current position within the Lepontine dome, the Adula Nappe underwent
235 several deformation phases. The oldest, peak to post-peak deformation phase is the eclogite facies
236 Zapport phase, which is well documented in the central part of the nappe, where it was not overprinted
237 by younger deformation phases (e.g. Löw, 1987; Meyre et al., 1993; Pleuger et al., 2003). The Zapport
238 phase records the earliest stages of exhumation and led to boudinage of the eclogite lenses, isoclinal
239 folding, an axial plane foliation, a N-S-trending stretching lineation, as well as a top-to-the-north sense of
240 shear (Meyre et al., 1993). Samples used for this study are from this area and represent deformed crustal
241 parts of the Alps.

242



244 Figure 2: Simplified tectonic map and north-south profile (along 730 line of longitude) of the Adula Nappe
245 in the Swiss coordinate system (modified after Nagel, 2008 and Cavargna-Sani et al., 2014). Grey and black
246 dots indicate poles of main foliation and stretching lineation, respectively, of the central Adula Nappe.
247 Sample locations are indicated. Swiss coordinates are marked in black; UTM coordinates are marked in
248 blue.

249

250 3. Methods

251

252 3.1. CPO analysis

253

254 CPO measurements were performed at the neutron time-of-flight (TOF) texture diffractometer SKAT at
255 the Frank Laboratory of Neutron Physics at JINR, Dubna, Russia (Ullemeyer et al., 1998; Keppler et al.,
256 2014). The high penetration capability of neutrons into matter together with the large beam cross section
257 of the SKAT (50 x 95 mm²) allow measurements of large-volume samples. In this study, roughly spherical
258 samples with volumes of about 65 cm³ were measured. Since the investigated samples are usually coarse-
259 grained this guarantees good grain statistics. Moreover, since diffraction patterns are recorded in a TOF
260 experiment over a large interval of lattice spacings, often containing hundreds of diffraction peaks, the so-
261 called 'Rietveld Texture Analysis' can be used for the texture evaluation, allowing the simultaneous
262 determination of all mineral textures even for samples with complex mineralogy (Von Dreele, 1997;
263 Matthies et al. 1997), as well as defining the rock mineral composition. We used the MAUD software for
264 the texture evaluation (Lutterotti et al., 1997; Wenk et al., 2010; Schmidtke et al., ~~submitted to same~~
265 ~~issue~~2021). For every sample, a sample coordinate system XYZ representing the three directions of the
266 finite strain ellipsoid was chosen. X is the lineation direction, Y is within the foliation plane perpendicular
267 to the lineation and Z is the foliation normal.

268

269 3.2. Modeling of elastic anisotropies

270

271 From the orientation distribution function (ODF) of the main rock constituents, their volume fractions in
272 each sample and particular single crystal elastic constants, the elastic moduli of bulk rock were calculated
273 using the BEARTEX software (Wenk et al., 1998). For that purpose, simple-averaging schemes are often
274 used, such as Voigt approach (Voigt, 1887) or Reuss approach (Reuss, 1929). The former assumes that all
275 crystallites in the polycrystal are under the same strain, while the latter considers equal stress state in all
276 crystallites. To get a first approximation on the different elastic anisotropy patterns within the set of
277 samples, we used the Voigt averaging scheme that provides reasonably good agreement of rock
278 petrofabric data and laboratory measurements (Ben Ismail and Mainprice, 1998), while noting that the
279 recalculated elastic properties represent the upper boundary of the polycrystal stiffness.

280 The single crystal elastic constants for the calculation were taken from the literature (muscovite: Vaughan
281 and Guggenheim, 1986; quartz: Heyliger et al., 2003; albite: Brown et al., 2006; calcite: Dandekar, 1968;
282 dolomite: Humbert & Plique, 1972; hornblende: Aleksandrov and Ryzhova, 1961; epidote: Aleksandrov et
283 al., 1974; garnet: Zhang et al., 2008; omphacite: Bhagat et al., 1992).

284 Phase elastic wave velocities were calculated from bulk elastic tensors of rocks using the Christoffel
285 equation.

286 To calculate the elastic anisotropy of the “average rock”, representative of ~~the upper~~ crustal lithology, and
287 its changes with overburden depth due to closure of the microcracks (see section 4.5), a more
288 sophisticated approach to the calculation of rock elastic properties is necessary. We used a modified self-
289 consistent method GeoMIXself (GMS; Matthies, 2010; 2012), which combines the standard self-consistent
290 routines (e.g. Morris 1970) with elements of the geometric mean averaging (Matthies & Humbert 1995).
291 This method is able to take CPO, morphologies and shape preferred orientations (SPOs) of grains, as well
292 as pores and cracks, into account. Similar to self-consistent approach, in GMS all rock constituents (mineral
293 grains, pores or microcracks) are approximated by oblate spheroids. Details and limitations of this
294 approach for an application to polymineral rocks are discussed in, e.g. ~~(Vasin et al., (2013), Vasin et al.,~~
295 (2017) and Lokajicek et al., (2021).

296

297 3.3. Ultrasonic measurements

298

299 From the sample set, two samples with common CPO patterns and strengths of their constituent mineral
300 phases were picked for ultrasonic measurements of P-wave velocity distributions at the pressure
301 apparatus of the Institute of Geology ASCR, Prague, Czech Republic (e.g. Lokajicek et al., 2014). The
302 measurements were conducted on spherical samples with diameters of 41.0 mm (RK15-17) and 39.4 mm
303 (RK15-22), respectively. Before the measurement, the samples were dried at 100°C for 24 hours.
304 Afterwards they were covered by a thin layer of epoxy resin to protect inner pore space of the sample
305 against the hydrostatic pressure. Transformer oil served as the hydraulic medium. Ultrasonic signals were
306 excited and recorded using a pair of piezoceramic sensors with a resonant frequency of 2 MHz. P-wave
307 velocities were measured during loading in 132 independent directions at differing confining pressure
308 levels from ambient conditions to a maximum pressure of 300 or 400 MPa.

309

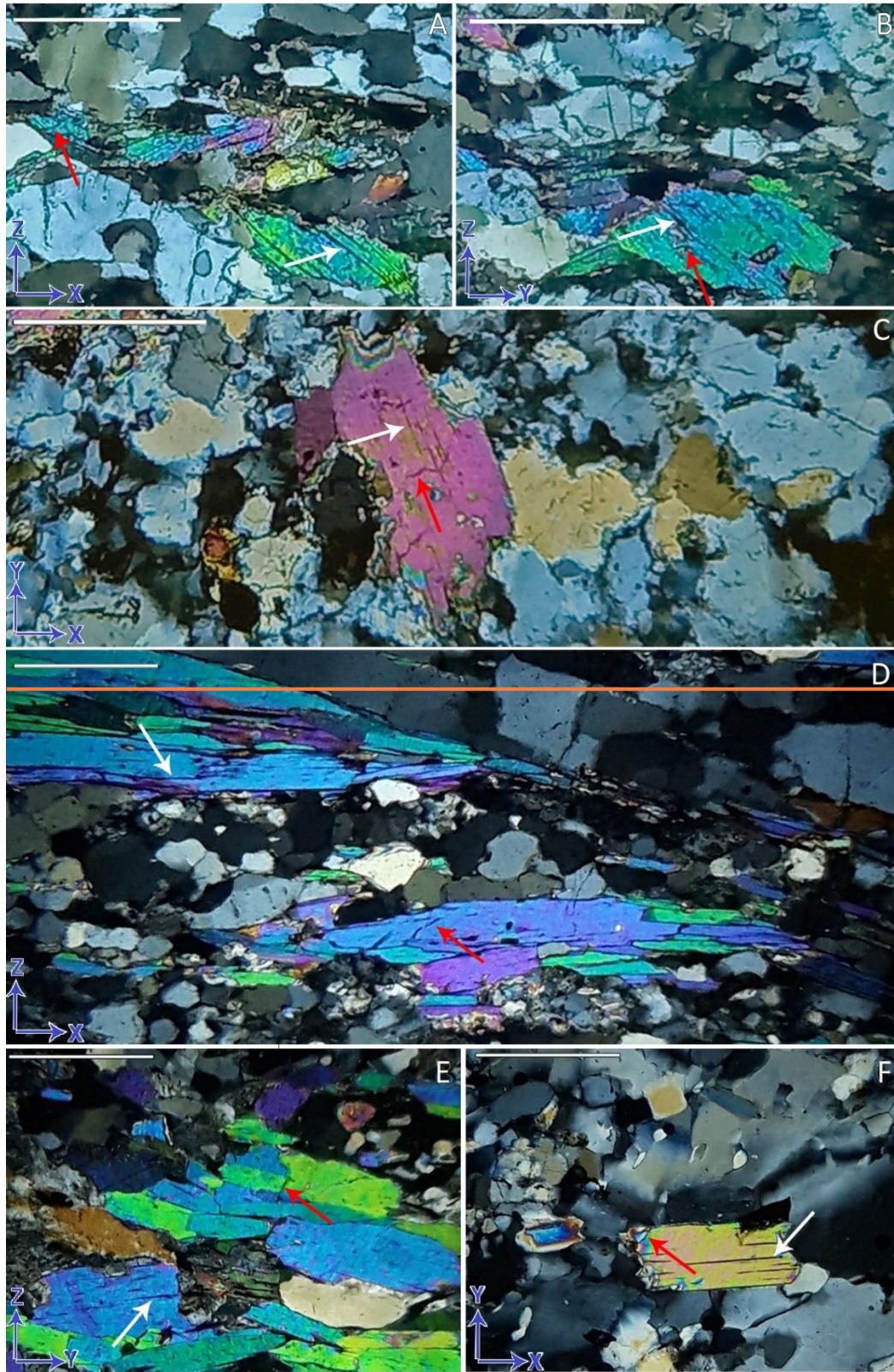
310 4. Results

311

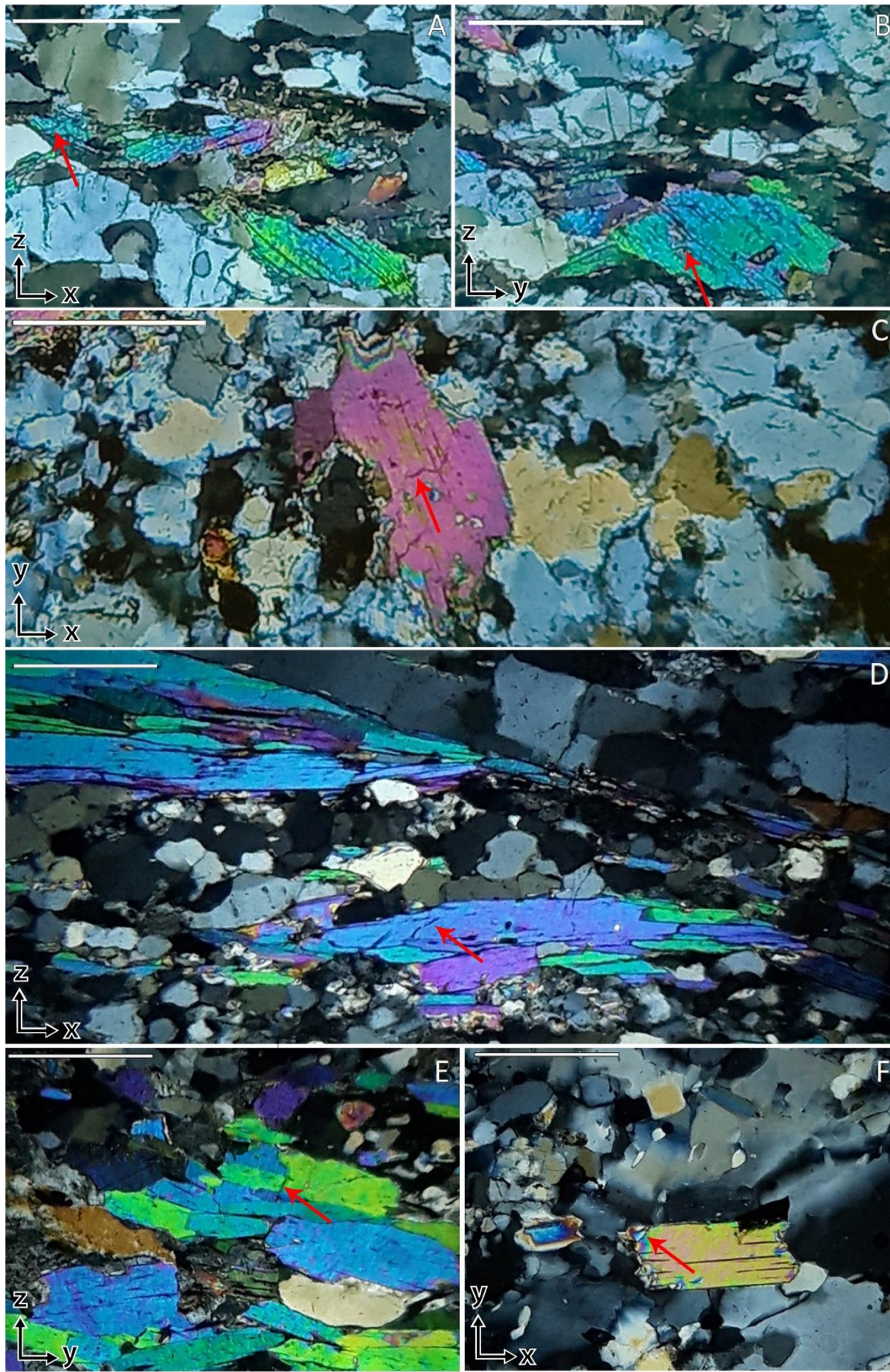
312 ~~4.1. Samples~~ description

313

314 The orthogneiss samples consist of quartz, plagioclase, ~~kalifeldspar~~ ~~potassium feldspar~~ and mica (Table 1A).
315 Mica is mostly white mica but a few samples also contain biotite. Mica is frequently aligned within the
316 foliation plane. It occurs in layers in some samples but exhibits single grains or clusters scattered within a
317 matrix of quartz and feldspar in most orthogneisses. Microcracks in mica grains are mostly aligned with its
318 basal plane, however there are also some microcracks cutting across basal planes (Fig 3A-C). Quartz ~~grains~~
319 exhibits signs the full range of dynamic recrystallization microstructures from -Grain boundary migration
320 to; subgrain rotation recrystallization and bulging.



321



323 Figure 3: Thin sections of [RK15-17](#), a typical orthogneiss (A, B, C) and [RK15-22](#), a typical
 324 paragneiss (D, E, F) under crossed polarizers for the XZ (A, D), YZ (B, E) and XY plane (C, F), showing examples microcracks
 325 ~~both parallel (white arrows) and oblique (red arrows) to the in mica basal planes.~~ ~~Blue arrows in left~~
 326 ~~corner~~ indicate the three directions of the finite strain ellipsoid. White bar on upper left corner in each
 327 picture shows the length of 500 μm .

A	Composition in Volume %	Location	B	Composition in Volume %	Location
GAN12	48 Qz, 31 Plg, 21 Kfs	Alp de Ganan	GAN08	36 Qz, 23 Plg, 31 Mica, 10 Grt	Alp de Ganan
JK6	39 Qz, 43 Plg, 18 Mica	720 652/155 999	GAN15	45 Qz, 26 Plg, 29 Mica	Alp de Ganan
MS17-15	25 Qz, 32 Plg, 11 Kfs, 32 Mica	732 692/140 078	MS17-12B	51 Qz, 20 Plg, 29 Mica	734 127/140 223
RK15-9A	71 Qz, 9 Plg, 20 Kfs	732 876/144 686	MS17-12C	32 Qz, 42 Plg, 26 Hlb	734 127/140 223
RK15-9B	60 Qz, 24 Plg, 15 Kfs, 1 Mica	732 876/144 686	RK15-5	60 Qz, 25 Plg, 15 Mica	732 933/142 432
RK15-10	71 Qz, 19 Plg, 10 Mica	733 398/151 952	RK15-18	16 Qz, 28 Plg, 56 Mica	730 110/142 903
RK15-11A	33 Qz, 32 Pl, 35 Kfs	722 272/152 194	RK15-22	55 Qz, 15 Plg, 30 Mica	729 771/139 042
RK15-17	35 Qz, 43 Plg, 22 Mica	729 661/143 839	RK60	25 Qz, 70 Plg, 5 Cc	726 875/152 275
RK15-20	50 Qz, 41 Plg, 9 Mica	730 265/140 481	RK68	50 Cc, 50 Dol	732 536/149 964
RK15-24B	38 Qz, 52 Plg, 14 Mica	730 008/136 819	RK70A	36 Qz, 38 Plg, 26 Mica	737 323/136 241
RK15-27B	63 Qz, 37 Plg	719 193/152 476	SADU16	42 Qz, 10 Plg 43 Mica, 5 Grt	732 641/134 758
RK15-28	34 Qz, 52 Plg, 14 Mica	719 424/153 347	SADU30	41 Qz, 25 Plg, 34 Mica	731 985/162 618
RK15-30B	29 Qz, 60 Plg, 11 Mica	727 713/156 013	ZAP01	29 Qz, 23 Plg, 37 Mica, 7 Grt, 4 Hbl	near Zapporthütte
RK15-31	76 Qz, 4 Plg, 20 Kfs	727 713/156 835			
RK63B	35 Qz, 32 Plg, 33 Kfs	731 539/148 966	C	Composition in Volume %	Location
RK66	37 Qz, 33 Plg, 30 Kfs	732 554/148 402	RK15-4	7 Qz, 29 Plg, 53 Hbl, 11 Omp	732 078/141 893
SADU39	58 Qz, 25 Plg, 17 Mica	733 687/139 694	RK15-7	15 Qz, 31 Plg, 51 Hbl, 3 Czo	732 467/143 492

328 Table 1: Sample locations in Swiss coordinates and mineral volume percentages of (A) orthogneisses, (B)
 329 paragneisses and (C) metabasites. Cc: calcite, Czo: clinozoisite, Dol: dolomite, Grt: garnet, Hbl: hornblende,
 330 Kfs: [Kalifeldspar](#)[kalifeldspar](#), Omp: omphacite, Plg: plagioclase, Qz: quartz.

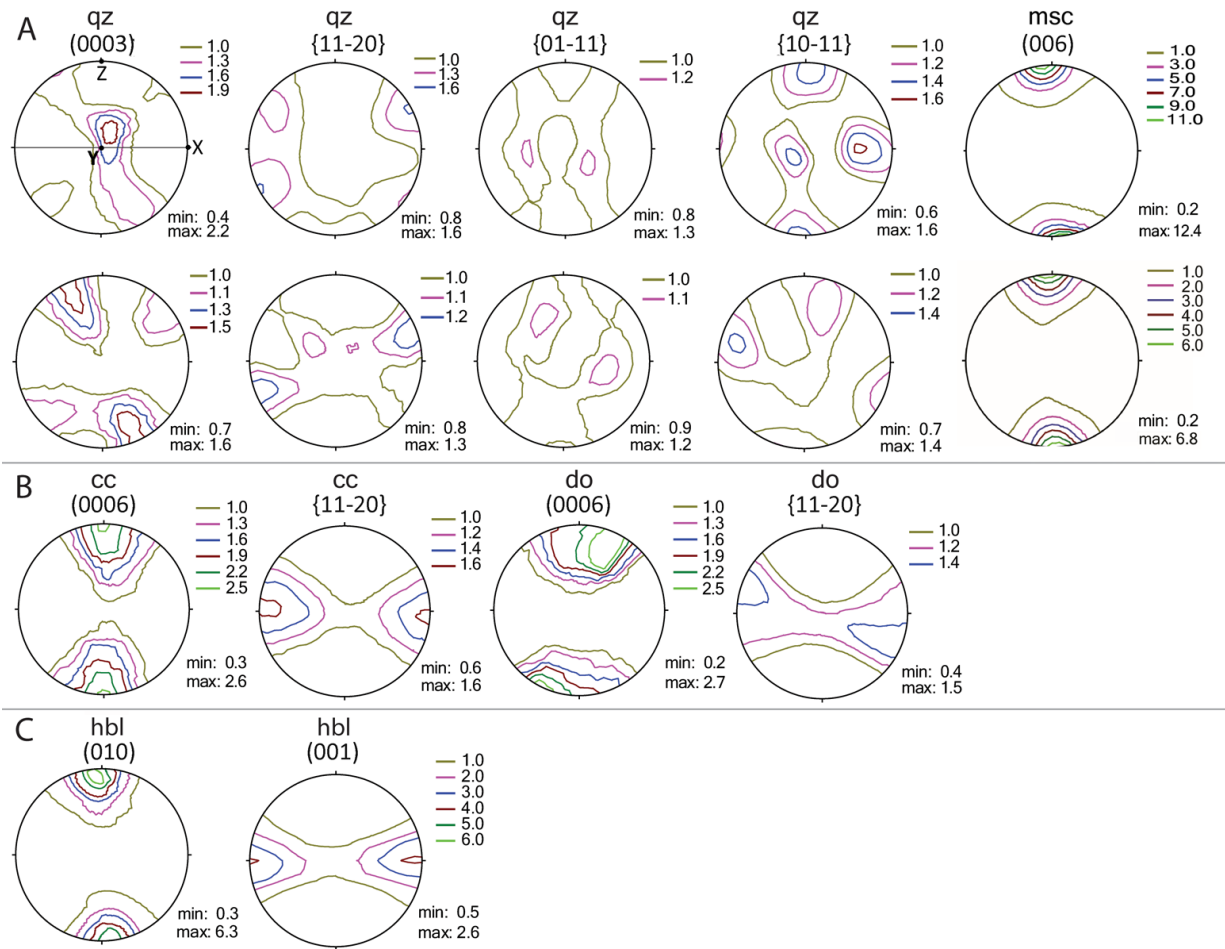
331
 332
 333 The mineral compositions of the paragneisses is more variable. Similar to the orthogneiss samples, the
 334 paragneisses consist of quartz, plagioclase and mica, however, there is no [kalifeldspar](#)[potassium feldspar](#)
 335 in the samples and the mica contents are generally higher (Table 1B). A few samples (RK15-18, SADU16)
 336 have a high mica content [of up to 56%](#) and [are](#) therefore [correctly termed](#) mica schists. [As](#)~~Since~~ they fall
 337 into the same category of clastic metasediments, they are [summarized as](#)~~counted among the~~ paragneisses
 338 which are the predominant rock type of that group. They were also considered for the calculation of the
 339 average sample, concerning composition and CPO. White mica is more common [within](#) the paragneisses
 340 [than in the orthogneisses.](#) ~~H~~however, [even](#) biotite occurs more frequently [in the paragneisses](#)~~than in the~~
 341 ~~orthogneisses~~. One of the paragneiss samples contains hornblende and several of the samples contain
 342 garnet. Mica appears more frequently aligned in layers compared to the orthogneisses. Microcracks are
 343 mostly parallel to the mica basal plane with some exceptions (Fig. 3D-F). Quartz microstructures ~~are~~ also
 344 [similar](#)~~correspond~~ to those of the orthogneisses.

345 The marble sample comprises equal amounts of calcite and dolomite, both of which exhibit an SPO with
 346 an alignment in the foliation. The metabasites are strongly retrogressed eclogites consisting of about 50%
 347 hornblende and variable amounts of quartz, plagioclase, omphacite and clinozoisite (Table 1C).
 348 Hornblende shows an alignment within the foliation plane and is preferentially oriented parallel to the
 349 stretching lineation.

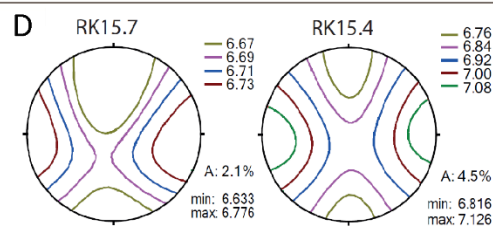
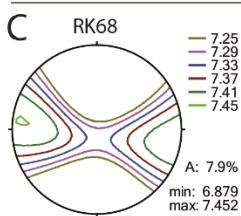
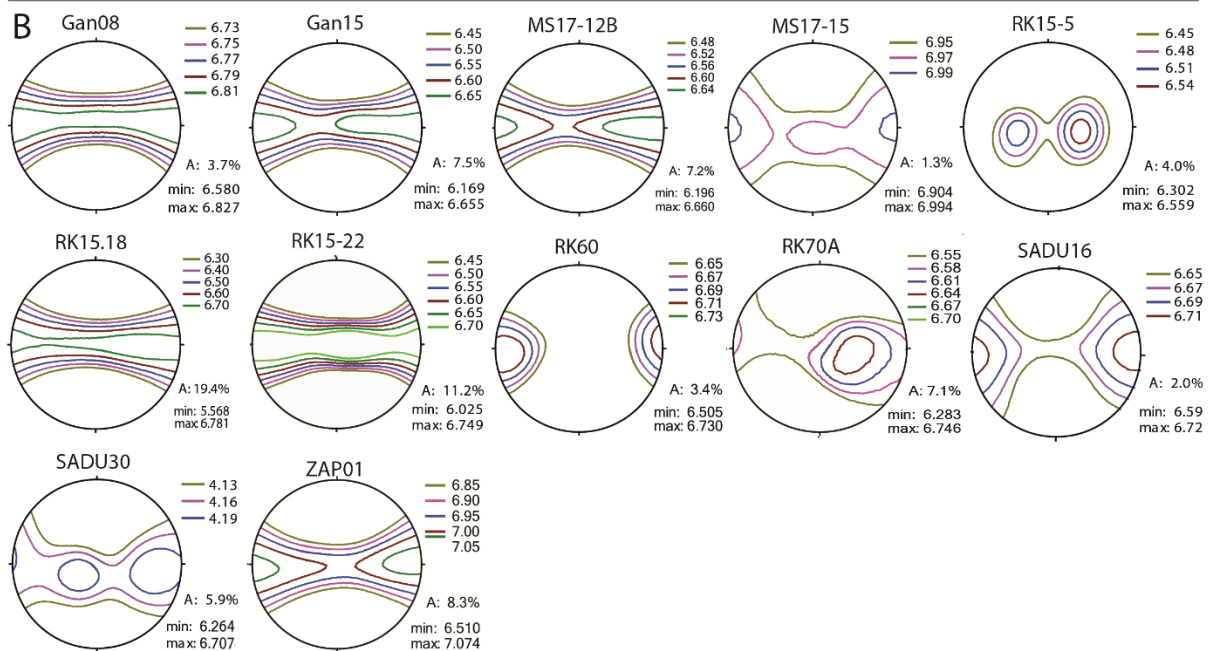
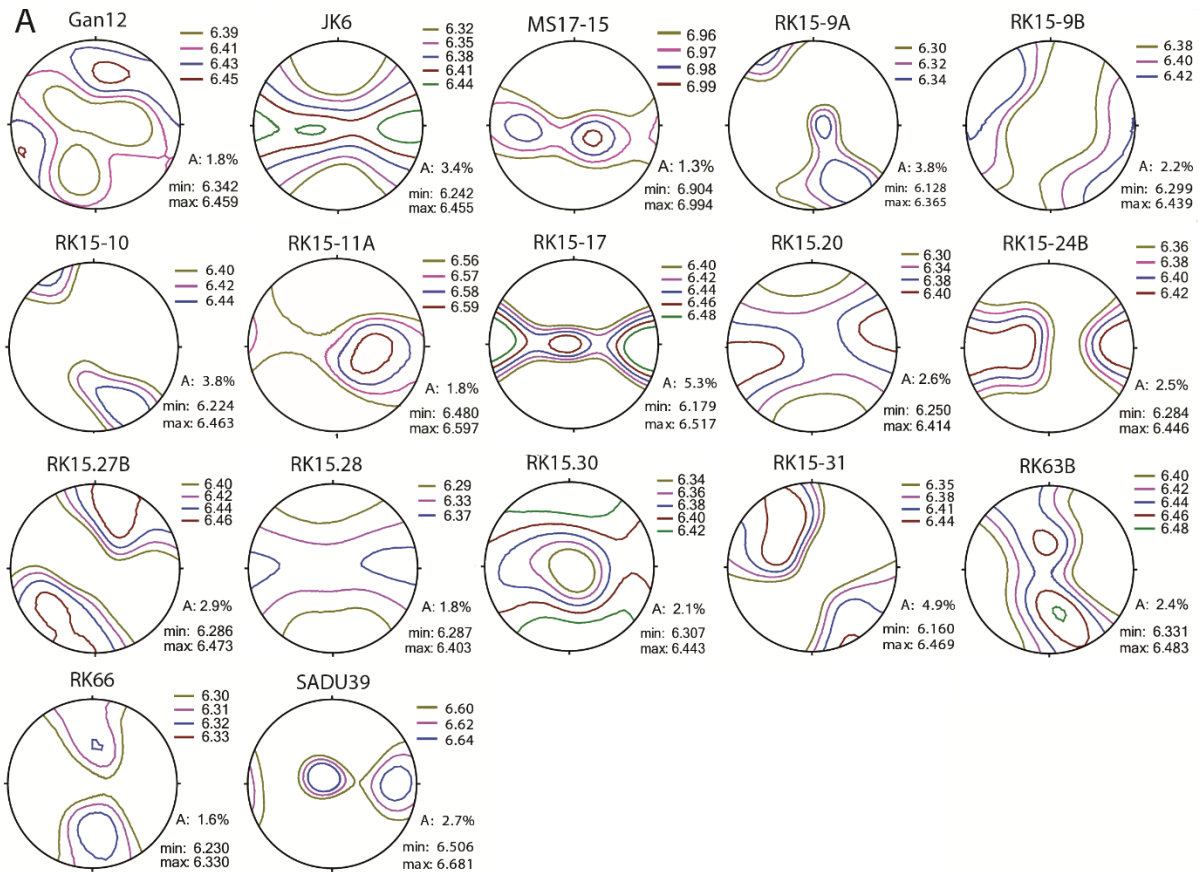
350
 351 [5. Results](#)

353 4.2.5.1. Crystallographic preferred orientation

354
355 Within the gneiss samples two major CPO patterns occur for quartz. In the first, quartz (0001) yields a
356 maximum between the Z- and Y-directions of the pole figure. This pattern occurs in 55% of the samples
357 containing quartz. In the second pattern, quartz (0001) exhibits peripheral maxima at an angle to the
358 foliation normal, occurring in 45% of the samples (Fig. 4A and APPENDIX). Both fabrics can contain
359 subordinate girdle distributions. Similar quartz (0001) fabrics have been described for other high pressure
360 gneiss samples (e.g. Kurz et al., 2002; Keller and Stipp, 2011; Keppler et al., 2015). Although the two ~~both~~
361 patterns occur throughout the sample set, the former is more common in the paragneisses, while the
362 latter occurs more frequently in the orthogneiss samples. In all samples quartz (0001) and (11-20) show
363 an asymmetry, which represents a sinistral motion indicating a top to the north sense of shear. This is in
364 accordance with literature and shows Zapport phase deformation in the Adula nappe (e.g. Löw, 1987;
365 Meyre et al., 1993; Pleuger et al., 2003). Different orientation patterns of quartz pole figures (10-11) and
366 (01-11) may be attributed to mechanical Dauphiné twinning, or induced by active rhombohedral slip (e.g.
367 Stipp and Kunze, 2008; Wenk et al., 2019). Both biotite and white mica show a strong CPO with a
368 pronounced alignment of their basal planes within the foliation in the gneiss samples (Fig. 4A). It should
369 be noted that in texture analysis (and in texture-based modeling of elastic properties) monoclinic crystals
370 are commonly defined in a first monoclinic setting (Matthies and Wenk, 2009), while a more common
371 second setting is used in this manuscript with (001) as a cleavage plane of mica. Both pagiolase and
372 ~~kalifeldspar~~ ~~feldspar~~ show a very weak to random CPO with only a few exceptions.
373 The marble sample yields a distinct calcite and dolomite CPO. Calcite exhibits an alignment of (0001) in Z-
374 direction and an alignment of (11-20) in X-direction (Fig. 4C). Both (0001) and (11-20) of dolomite show an
375 angle to the Z- and Y-direction respectively. In the metabasites, hornblende is the only mineral yielding a
376 pronounced CPO (Fig. 4D). It shows a strong alignment of (010) in Z-direction and (001) in X-direction in
377 both samples.



378
 379 Figure 4: CPO types in the sample set (A) Common quartz (top: RK15-28; bottom: JK6) and mica (top: RK15-
 380 5; bottom: RK15-28) CPO in the orthogneisses and paragneisses; (B) calcite and dolomite CPO in the marble
 381 sample (RK68); (C) typical hornblende CPO in the metabasites (RK15-4). All pole figures are lower
 382 hemisphere equal area projections. The foliation normal (Z) is vertical, the lineation (X) is horizontal and
 383 north is left.



385 Figure 5: Modelled P-wave anisotropies of all natural samples in equal area stereographic projection. (A)
 386 Orthogneisses; (B) paragneisses ; (C) marble and (D) metabasites. Contour lines, as well as minima and
 387 maxima are in km/sec. The foliation is perpendicular to the projection plane, the lineation is horizontal.
 388 XYZ orientation is the same as in Fig. 4.

389

390 4.3.5.2. Modeled elastic anisotropies of natural samples

391

392 5.2.4.3.1. Orthogneisses

393

394 P-wave anisotropies-anisotropy (AV_p) is defined as $A = (V_p \text{max} - V_p \text{min}) / V_p \text{mean} * 100\%$. The orthogneisses
 395 show two main patterns, one of which yields highest P-wave velocity (V_p) at an angle to the foliation
 396 normal, the other exhibits a V_p maximum in the lineation direction with a distribution of high V_p values in
 397 the foliation plane in some samples (Fig. 5A). The maxima at an angle to the foliation normal are frequently
 398 elongated or even show two distinct maxima within an area of higher V_p (GAN12, RK15-9A, RK15-27B).
 399 Only few samples deviate from these two patterns showing maxima between the Y direction and the
 400 foliation normal (RK63B, RK66) or several maxima within the foliation plane (MS17-15, SADU39). AV_p lies
 401 between 1.3 and 5.3% with an average of 2.9%. V_p/V_s ratios are between 1.51 and 1.67 (Table 2A) with an
 402 average of 1.60.

403

A	Vp A (%)	Vs1 A (%)	Vs2 A (%)	VP/Vs	Vp (km/s)	Vs (km/s)	B	Vp A (%)	Vs1 A (%)	Vs2 A (%)	VP/Vs	Vp (km/s)	Vs (km/s)
GAN12	2,5	1,8	1,7	1,57	6,40	4,07	GAN08	3,7	5,0	1,4	1,64	6,73	4,11
JK6	3,4	2,0	3,0	1,63	6,35	3,91	GAN15	7,5	6,7	4,5	1,58	6,43	4,07
MS17-15	1,3	1,0	0,5	1,63	6,95	4,27	MS17-12B	7,2	5,7	3,3	1,57	6,44	4,10
RK15-10	3,8	3,1	2,4	1,53	6,35	4,16	MS17-12C	2,0	1,2	1,2	1,65	6,61	4,01
RK15-11A	1,8	1,0	1,2	1,61	6,55	4,06	RK15-18	20,5	19,4	11,5	1,65	6,18	3,73
RK15-17	5,3	5,0	2,5	1,65	6,35	3,86	RK15-22	11,2	8,0	5,5	1,56	6,42	4,10
RK15-20	2,6	1,5	1,1	1,60	6,33	3,96	RK15-5	4,3	4,0	1,9	1,55	6,42	4,14
RK15-24B	2,5	1,8	2,1	1,64	6,37	3,89	RK60	3,4	2,8	1,5	1,64	6,60	4,03
RK15-27B	2,9	3,6	2,3	1,54	6,39	4,14	RK68	7,9	4,4	2,3	1,82	7,22	3,96
RK15-28	1,8	1,1	1,6	1,64	6,35	3,86	RK70A	7,1	6,1	4,3	1,61	6,53	4,06
RK15-30B	2,1	1,0	0,6	1,67	6,39	3,81	SADU16	2,0	1,5	1,0	1,60	6,65	4,15
RK15-31	4,9	5,4	3,6	1,51	6,33	4,18	SADU30	6,8	5,9	2,7	1,60	6,50	4,07
RK15-9A	3,8	3,2	3,5	1,54	6,26	4,06	ZAP01	8,3	6,6	3,3	1,64	6,81	4,17
RK15-9B	2,2	1,5	1,5	1,57	6,38	4,07							
RK63B	2,4	1,6	1,9	1,63	6,42	3,95	C	Vp A	Vs1 A	Vs2 A	VP/Vs	Vp	Vs
RK66	1,6	1,1	0,8	1,64	6,29	3,83	RK15-4B	4,5	1,7	1,2	1,79	6,94	3,88
SADU39	3,1	2,7	2,0	1,56	6,57	4,21	RK15-7	2,1	0,6	0,7	1,76	6,70	3,81

404

405 Table 2: P-wave and S-wave anisotropy, VP/VS ratio as well as Voigt average of P-wave and S-wave
 406 velocities of (A) orthogneisses, (B) metasediments and (C) metabasites.

407

408 5.2.4.3.2. Paragneisses

409

410 The paragneiss samples all show highest V_p value within the foliation plane (Fig. 5B). Most samples also
 411 yield a maximum in the lineation direction. There are two samples displaying maxima within the foliation
 412 plane but not aligned in the lineation direction (RK15-5; SADU30). The AV_p of the paragneisses is highly
 413 variable ranging from 2.0% to 20.5% (Table 2B). Most samples, however, show a moderate AV_p of 7-8%.
 414 V_p/V_s ratios lie between 1.55 and 1.65.

415

416 5.2.4.3.3. MarbleMinor lithologies

417

418 The marble sample RK68 exhibits an AV_p of 7.9% with a maximum at a smalllight angle to the lineation
419 direction and some distribution of high V_p values in the foliation plane (Fig. 5C). Its V_p/V_s ratio is 1.82 (Table
420 2B).

421

422 5.2.4.3.3. Metabasites

423

424 The V_p distributions in the metabasites show a pronounced maximum in the lineation direction (Fig. 5
425 D). Lowest V_p is found parallel to the foliation normal. AV_p values are 4.5% and 2% with V_p/V_s ratios of 1.79
426 and 1.76, respectively (Table 2C).

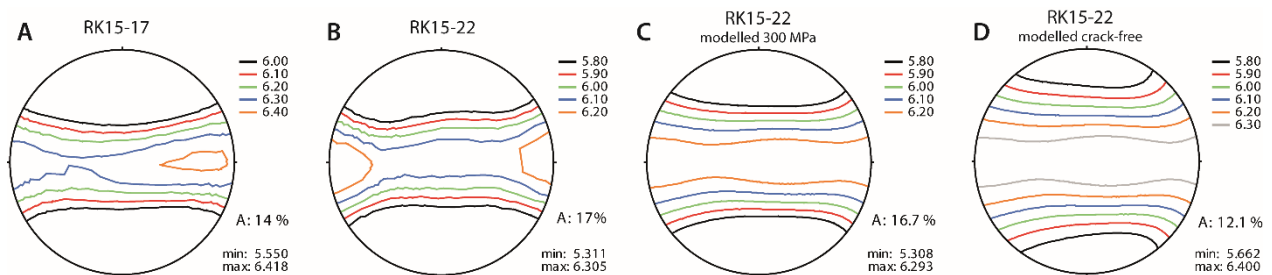
427

428 4.4.5.3. Measured elastic anisotropies of natural samples

429

430 The V_p distribution of the two gneiss samples, which were measured using ultrasound at different confining
431 pressures both show high V_p in the foliation plane. The orthogneiss RK15-17 yields a maximum V_p within
432 the foliation plane at a slight angle to the lineation (Fig. 6A). At maximum pressures of 400 MPa its AV_p is
433 14%. The paragneiss RK15-22 was measured at a maximum pressure of 300 MPa. Maximum V_p is aligned
434 in the lineation direction (Fig. 6B). It exhibits an AV_p of 17%. Both samples show increasing V_p values as
435 well as decreasing AV_p coefficients with increasing pressures during the experiment (Table 3). In general,
436 the RK15-17 orthogneiss is elastically more isotropic and shows V_p values comparable to the RK15-22
437 paragneiss at pressures over 100 MPa (Table 3), but at lower pressures P-wave velocities in the orthogneiss
438 decrease drastically, and the elastic anisotropy significantly increases, reaching values much higher than
439 in the paragneiss.

440



441

442 Figure 6: P-wave anisotropies of (A) an (A) orthogneisses (RK15-17) and (B) a (B) paragneiss (RK15-22)
443 measured using ultrasounding. Figures show P-wave distribution at maximum pressures in the
444 experiments. V_p distribution of RK15-22 modelled with GMS algorithm at 300MPa (C) and at crack-free
445 pressures (D). Contour lines, as well as minima and maxima are in km/sec. XYZ orientation is the same as
446 in Figs. 4 and, 5.

447

448 4.5.5.4. "Average" rock concept and crack-free "average" rock

449

450 Elastic properties and elastic wave velocities in rocks are normally assessed in laboratory measurements
451 on samples of several cm length. To implement elastic anisotropies in geophysical models these

laboratory-derived elastic properties need to be upscaled to a km scale. It is necessary to calculate elastic properties of the rock massif in a long-wavelength approximation (Berryman, 1980), and thus a whole rock massif may be represented as an effective “average” rock. It should feature average CPOs, volume fractions and grain shapes of minerals, as well as average pore and crack patterns. Of course one needs to bear in mind that even in these larger massifs heterogeneities like the aforementioned lenses and layers of different lithologies exist.

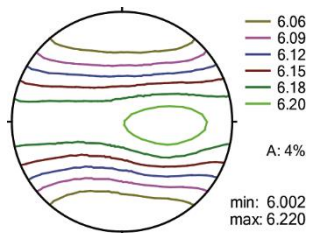
	A RK15-17, experiment			B RK15-22, experiment			C RK15-22, model					
Pressure (MPa)	V_{Pmin} (km/s)	V_{Pmax} (km/s)	AV_P (%)	V_{Pmin} (km/s)	V_{Pmax} (km/s)	AV_P (%)	V_{Pmin} (km/s)	V_{Pmax} (km/s)	AV_P (%)	Type I crack density	Type II crack density	Total crack porosity
0				2.876	5.062	53						
2				3.292	5.134	43						
10	2.637	4.459	51	3.904	5.349	31	3.904	5.350	31	0.205	0.056	0.0145
20	3.207	4.812	40	4.194	5.520	27	4.196	5.524	27	0.162	0.048	0.0118
50	4.106	5.316	26	4.584	5.786	23	4.583	5.791	23	0.112	0.031	0.0079
100	4.787	5.824	20	4.902	6.019	20	4.915	6.037	20	0.074	0.014	0.0046
200	5.307	6.203	16	5.202	6.269	19	5.213	6.263	18	0.043	0	0.0018
300	5.501	6.339	14	5.311	6.305	17	5.307	6.293	17	0.033	0	0.0014
400	5.550	6.418	14									
Crack free							5.662	6.400	12	0	0	0

	RK15-17, experiment			RK15-22, experiment			RK15-22, model					
Pressure (MPa)	V_{Pmin} (km/s)	V_{Pmax} (km/s)	AV_P (%)	V_{Pmin} (km/s)	V_{Pmax} (km/s)	AV_P (%)	V_{Pmin} (km/s)	V_{Pmax} (km/s)	AV_P (%)	Type I crack density	Type II crack density	Total crack porosity
5				3.656	5.242	35	3.662	5.244	36	0.246	0.057	0.0163
10	2.637	4.459	51	3.904	5.349	31	3.904	5.350	31	0.205	0.056	0.0145
20	3.207	4.812	40	4.194	5.520	27	4.196	5.524	27	0.162	0.048	0.0118
50	4.106	5.316	26	4.584	5.786	23	4.583	5.791	23	0.112	0.031	0.0079
100	4.787	5.824	20	4.902	6.019	20	4.915	6.037	20	0.074	0.014	0.0046
200	5.307	6.203	16	5.202	6.269	19	5.213	6.263	18	0.043	0	0.0018
300	5.501	6.339	14	5.311	6.305	17	5.307	6.293	17	0.033	0	0.0014
400	5.550	6.418	14									
Crack free							5.662	6.400	12	0	0	0

Table 3: Results of ultrasonic measurements of (A) orthogneiss RK15-17 and (B) paragneiss RK15-22 showing V_P and AV_P at increasing pressures. (C) V_P and AV_P of RK15-22 modelled with GMS algorithm.

As a first approximation to the crustal properties, only major minerals were considered for the “average” rock: plagioclase, muscovite and quartz. Minor or uncommon mineral phases were omitted. From the selection of 30 natural crustal rocks, we identified characteristic CPO types and average CPO strengths for all common mineral phases. In general, feldspar shows weak to random CPO, even in strongly deformed samples. Furthermore, only minor differences have been observed between plagioclase and potassium kalifeldspar. Therefore, the ODF of a representative plagioclase with weak texture was chosen for the “average” rock, namely, the albite ODF in RK15-28 sample. Since white mica is most common in both orthogneisses and paragneisses, muscovite was chosen as representative mica for the average rock. In all samples mica shows a pronounced alignment of its basal plane in the foliation. The mica ODF of two samples (RK15-5; RK15-28) was combined in 1:1 ratio to yield an average preferred orientation for the “average” sample. Likewise, the representative quartz ODF for the average sample was chosen as a combination of CPOs from two different samples (JK6; RK15-28) in 5:6 ratio, based on the frequency of occurrence of each CPO pattern in the sample set. These two samples show the typical quartz CPO patterns mentioned in section 4.4 and shown in Fig. 4A.

478 Based on the analysis of all samples, average mineral volume percentages in gneisses (43% quartz, 40%
 479 plagioclase, 17% mica) were considered for the “average” rock. Corresponding density value is 2670.7
 480 kg/m³. For the GMS method, grain shapes of minerals should be approximated by ellipsoids. Thin section
 481 analysis of samples revealed more or less equiaxed grain shapes of quartz and feldspar and elongated mica
 482 platelets with average aspect ratio of ≈0.2 (APPENDIX – Fig 1). Numerical models revealed that aspect
 483 ratios of grains of mica and quartz within 0.1-1 range have only minor influence on bulk elastic properties
 484 (Nishizawa and Yoshino, 2001; Vasin et al., 2013; Huang et al., 2021). Consequently, for the “average” rock,
 485 we considered spherical grains of quartz and feldspar, and oblate spheroidal grains with axes ratio 1:1:0.2
 486 for mica. As the shape of mica grains is related to cleavage, the corresponding SPO may be derived from
 487 the CPO by considering additional rotation of the crystallite coordinate system (Vasin et al., 2013).
 488 The preferred orientations, mineral volume fractions and grain shapes were combined in a model of the
 489 elastic properties for the “average” rock using the GMS approach. The V_P distribution in a crack-free
 490 “average” rock is shown in Figure 7. There is a distribution of high V_P values within the foliation plane, and
 491 the maximum V_P direction is located between the lineation (X-direction) and the Y-direction. The AV_P of
 492 the “average” crack-free gneiss is 4%.
 493 This “average” rock would be found at depths of at least 28 km, which means that considering an average
 494 crustal thickness most of the crust would be above this point. This is why it is also important to consider
 495 the microcrack pattern in such an average rock at lower depth.
 496



497
 498 Figure 7: Modelled P-wave anisotropies of an average gneiss at 740 MPa. Contour lines, as well as minima
 499 and maxima are in km/sec. XYZ orientation is the same as in Fig. 4.

500
 501 4.6.5.5. “Average” rock with microcrack systems

502
 503 As directly evident from thin sections analysis (Figure 3), low aspect ratio microcracks are present in the
 504 samples. At low overburden depths, these microcracks are open. As seen from Table 3, at low pressures
 505 measured elastic wave velocities are decreased and elastic anisotropy is increased compared to the high
 506 pressure, where the majority of microcracks are-is closed. To account for the changes inof elastic
 507 anisotropy of the “average” rock due to pressure/depth changes, it is necessary to include these
 508 microcracks and their closure with increasing pressure into the model.
 509

Pressure (MPa)	Depth (km)	Density (kg/m ³)	Type I crack density	Type II crack density	Total crack porosity	V_{pmin} (km/s)	V_{pmax} (km/s)	AV _p (%)
5	0.2	2627.19	0.246	0.057	0.0163	4.203	4.728	12
10	0.4	2631.99	0.205	0.056	0.0145	4.442	4.891	10
20	0.8	2639.21	0.162	0.048	0.0118	4.721	5.121	8
50	1.9	2649.62	0.112	0.031	0.0079	5.077	5.454	7
100	3.8	2658.43	0.074	0.014	0.0046	5.372	5.748	7
200	7.6	2665.91	0.043	0	0.0018	5.630	6.012	7
300	11.5	2666.98	0.033	0	0.0014	5.709	6.057	6
≈740	28.2	2670.72	0	0	0	6.002	6.220	4

510
511 Table 4: V_p , AV_p, and crack densities of “average” rock model at increasing pressures ~~including and~~
512 corresponding depth. 740 MPa is an estimation of the pressure where the cracks are closed (see text).
513 Cracks type I have the same ODF as mica.

514
515 As a first approximation, we considered that the “average” rock should have the same crack distribution
516 as one of the characteristic gneiss samples, i.e., sample RK15-22. From thin sections analysis (Figure 3D-
517 F), two possible microcrack systems were identified. There is one set of microcracks mostly oriented along
518 the muscovite platelets, and we denote ~~these this set~~ as type I cracks. Type I cracks were assumed to have
519 the same SPO as muscovite grains; and their aspect ratio was estimated to be ≈0.01 (Appendix – Fig 2). As
520 these cracks are roughly parallel to mica platelets, within the GMS algorithm type I cracks were
521 approximated by oblate ellipsoids with an axial ratio of 1:1:0.01. Another set of cracks – denoted as type
522 II cracks - intersects quartz grains, ~~These cracksthey~~ are mostly oriented parallel to the Z axis. They display
523 a broader range of aspect ratios with an average of ≈0.025 (Appendix – Fig 1). Since these cracks are mostly
524 within equiaxed quartz grains, they were approximated by oblate ellipsoids with an axial ratio of 1:1:0.025.
525 To determine the changes of crack densities of type I and II with pressure, ~~thea~~ following procedure was
526 applied.

527 Elastic properties of a crack-free RK15-22 gneiss were modelled with GMS algorithm using measured ODFs,
528 mineral volume fractions (55% quartz, 15% albite and 30% muscovite), and assuming spherical grain
529 shapes for quartz and albite, and 1:1:0.2 ellipsoidal grains for muscovite. Using mineral density values from
530 the same references as mineral single crystal elastic properties, a density of 2702.3 kg/m³ was computed
531 for a crack-free RK15-22. Using model elastic properties and this density value, the V_p distribution in a
532 crack-free RK15-22 was calculated (Fig. 6C).

533 Density measurements of RK15-22 at atmospheric pressure yield a value of 2658 kg/m³. Thus, crack
534 porosity in RK15-22 is restricted to a maximum of about ~1.7%. Consequently, type I and type II cracks
535 were added into the model crack-free RK15-22 gneiss to reproduce measured V_p distributions at different
536 pressures, similar to the procedure of porous polycrystalline graphite (Matthies, 2012). The only varying
537 parameters are the type I and type II crack porosities, with the total crack porosity within the
538 aforementioned limit. Using this procedure, an adequate description of experimental V_p distributions with
539 the GMS approach was achieved at all pressures above 2 MPa. The wave velocities and AV_p values of RK15-
540 22 models are given in Table 3.

541

Pressure (MPa)	C ₁₁ (GPa)	C ₁₂ (GPa)	C ₁₃ (GPa)	C ₁₄ (GPa)	C ₁₅ (GPa)	C ₁₆ (GPa)	C ₂₂ (GPa)	C ₂₃ (GPa)	C ₂₄ (GPa)	C ₂₅ (GPa)	C ₂₆ (GPa)	C ₃₃ (GPa)	C ₃₄ (GPa)	C ₃₅ (GPa)	C ₃₆ (GPa)
5	58.0	9.1	7.8	0.1	-0.1	-0.2	58.1	7.9	0.2	-0.1	-0.3	46.4	0.1	-0.1	0.0
10	62.2	10.2	9.0	0.1	-0.1	-0.2	62.4	9.0	0.2	-0.1	-0.3	51.9	0.1	-0.1	0.0
20	68.4	11.8	10.6	0.1	-0.1	-0.2	68.6	10.6	0.2	-0.1	-0.3	58.8	0.1	-0.1	0.0
50	77.9	14.6	13.3	0.1	0.0	-0.2	78.2	13.3	0.2	-0.1	-0.3	68.3	0.1	-0.1	0.0
100	86.8	17.5	16.1	0.1	0.0	-0.1	87.1	16.2	0.2	-0.1	-0.4	76.7	0.1	-0.1	0.0
200	95.2	20.7	19.1	0.1	0.0	-0.1	95.6	19.1	0.2	-0.1	-0.4	84.5	0.0	-0.1	0.0
300	96.7	21.3	19.8	0.1	0.0	-0.1	97.1	19.9	0.2	-0.1	-0.4	86.9	0.0	-0.1	0.0
≈740	102.2	23.7	22.9	0.0	0.1	-0.1	102.6	23.0	0.1	-0.1	-0.4	96.2	0.0	-0.1	0.0

continuation

Pressure (MPa)	C ₄₄ (GPa)	C ₄₅ (GPa)	C ₄₆ (GPa)	C ₅₅ (GPa)	C ₅₆ (GPa)	C ₆₆ (GPa)
5	21.5	-0.1	-0.1	21.4	0.1	24.6
10	23.4	-0.1	-0.1	23.2	0.1	26.2
20	25.8	-0.1	-0.1	25.6	0.1	28.5
50	29.1	-0.1	-0.1	28.9	0.1	31.9
100	32.0	-0.1	-0.1	31.7	0.1	35.0
200	34.5	-0.1	-0.1	34.2	0.1	37.7
300	35.1	-0.1	-0.1	34.8	0.1	38.1
≈740	37.3	-0.1	-0.1	36.9	0.1	39.7

542

543 Table 5: Bulk elastic tensor components of the “average” rock model, rounded to first decimal digit.

544

545 At maximum pressure of 300 MPa the experimental V_p values are 0.3-0.7 km/s lower than corresponding
546 velocities in the crack-free RK15-22 with biggest differences for minimum velocities. This implies a small
547 amount of open microcracks in the experiment. Modeling suggests that type II cracks with 0.025 aspect
548 ratio are not necessary to describe bulk elastic properties of RK15-22 sample at pressures of 200 MPa and
549 higher. Thus, we assume that type II crack porosity is close to zero at 300 MPa. Since type I cracks
550 orientation distribution is not random, and the material is elastically anisotropic with $AV_p = 17\%$, only a
551 rough estimation of type I cracks closure pressure can be made. We averaged the stiffness tensor of crack-
552 free RK15-22 over all directions and applied the relation derived by Walsh (1965) for an isotropic rock to
553 obtain a closure pressure of ≈740 MPa for type I cracks at an aspect ratio of 0.01. Thus, we assume that
554 the RK15-22 gneiss may be considered crack free at a pressure of 740 MPa.

555 It is recognized that at low crack porosities effective elastic properties of the material depend on the crack
556 density, while crack porosity is irrelevant (Vernik, 2016; Kachanov and Mishakin, 2019). Crack porosity and
557 crack density may be related for certain types and distributions of cracks. E.g., in the case where all cracks
558 have the same aspect ratio, as type I or type II pores separately, there is a simple equation (Lokajicek et
559 al., 2021) connecting crack porosity and crack density. Thus, in Table 4, crack densities are given for type I
560 and type II cracks separately, as well as the total crack porosity. We assume that the same system of cracks
561 exists in an “average” sample such as RK15-22, with the same orientation distribution and the same crack
562 density values at corresponding confining pressure. The GMS algorithm was used to add this crack system
563 to the crack-free “average” rock, and the density of the crack-free “average” rock was used to estimate
564 the overburden from the pressure values. From that, the dependencies of all stiffness tensor components
565 of the “average” rock on depth were obtained, as well as the elastic wave velocities and the AV_p
566 coefficients (Tables 4 and 5).

567 We note that the proposed model is aimed to reproduce ultrasonic wave velocities measured during
568 sample loading. It may be expected that during unloading, ultrasonic wave velocities would be higher at
569 same pressure levels due to irreversible closure of some microcracks. This effect would certainly adjust

570 [the depth estimates, but it may also change the rock anisotropy if the mechanism of irreversible closure is](#)
571 [different for type I and type II cracks. The effect of crack closure should be studied in more detail with](#)
572 [respect to rock massif.](#)

573

574 [5.6.](#) Discussion

575

576 There are various factors influencing the elastic anisotropy of rocks. While the deformation-induced CPO
577 is the main cause, there are other aspects like shape preferred orientation (SPO) of grains, or layering
578 contributing to elastic anisotropy. Another important factor influencing elastic anisotropy, especially at
579 lower depth is the occurrence of microcracks. In the following, we discuss the elastic anisotropies -
580 calculated and measured - of the natural samples from this study. We will elaborate the applicability of
581 the model “average” rock to larger scale crustal rock units and [critically assess](#)~~discuss~~ the controlling
582 factors of the elastic anisotropy of crustal rocks.

583

584 [5.6.1.](#) Elastic anisotropy of natural samples

585

586 [5.6.1.1.](#) Orthogneisses

587

588 The AV_p calculated from the CPO data of orthogneisses is largely influenced by CPOs of quartz and mica.
589 Since feldspar generally shows weak or no CPO, its presence in the samples mainly contributes to a
590 decrease in AV_p . Mica adds to increased V_p values within the foliation plane as well as the maxima in [the](#)
591 lineation direction in some samples. Highest V_p is found within the basal plane of mica single crystals,
592 which defines the V_p pattern caused by observed alignment of mica basal planes within the foliation. The
593 maxima in [the](#) lineation direction are caused by a slight tilting of mica basal planes around the lineation.
594 This leads to broadening of high V_p region within the YZ-plane and results in the highest V_p in lineation
595 direction. Highest V_p values of quartz single crystals are observed close to normals to their rhombohedral
596 planes. Patterns showing elongated V_p maxima close to the periphery at an angle to the foliation and the
597 patterns with several maxima for V_p are due to the influence of quartz CPO. The frequently observed
598 asymmetry in these patterns with respect to the reference frame of foliation and lineation reflects non-
599 coaxial deformation of the rocks. All units in the central Adula Nappe show a top-to-the-north sense of
600 shear (e.g. Nagel, 2008), thereby producing asymmetric quartz CPO, which in turn leads to the asymmetric
601 V_p distributions in the mica-poor orthogneisses. Both AV_p as well as V_p patterns are similar to those in
602 previous studies, which either show high V_p in the foliation with a maximum in [the](#) lineation direction
603 (Ivankina et al. 2005; Ullemeyer et al., 2006; Kern et al. 2008; Zel et al., 2015; Ivankina et al., 2017;
604 Schmidtke et al., ~~submitted to same issue~~2021), at an angle to the lineation (Vasin et al., 2017), or
605 elongated asymmetric maxima between the foliation normal and the foliation plane (Ullemeyer et al.,
606 2006; Llana-Fúnez et al., 2009).

607 The orthogneiss sample RK15-17 measured in the lab shows high V_p distributed within the foliation plane
608 with a maximum at a slight angle to [the](#) lineation direction. While both the measured and the calculated
609 velocity patterns for this sample show high V_p distributed in the foliation plane, the AV_p pattern calculated
610 from CPO yields its maximum aligned in [the](#) lineation direction with an additional maximum in Y-direction.
611 The AV_p coefficient calculated from measured P-wave velocities at a pressure of 400 MPa is higher than

612 the calculated one by a factor 2.6, which is mostly due to still open microcracks, not considered within the
613 Voigt averaging scheme. Due to a preferred orientation of microcracks parallel to the mica basal plane
614 (Fig. 3A-C) and an alignment of mica in the foliation V_p is slower normal to the foliation and AV_p is higher
615 in the samples measured in the lab, even at the highest pressures.
616 V_p/V_s ratios in the orthogneiss samples are influenced by the volume percentage of the constituent mineral
617 phases. Due to the low Poisson ratio of quartz and its generally large volume percentage in the
618 orthogneisses their V_p/V_s ratios of 1.51-1.67 are low.

619

620 5.6.1.2. Paragneisses

621

622 Like in the orthogneisses, the V_p pattern of the paragneisses and mica schists is influenced by mica and
623 quartz CPO with a larger mica contribution due to its generally higher volume content in paragneisses
624 compared to the orthogneisses (Table 1B). Likewise, mica CPO leads to high V_p values within the foliation
625 plane and frequently to a V_p maximum in the lineation direction. This V_p pattern is similar to that of
626 paragneisses in previous studies (e.g. Weiss et al., 1999; Erdman et al., 2013; Keppler et al., 2015;
627 Ullemeyer et al., 2018). V_p patterns showing maxima within the foliation plane, but not aligned with the
628 lineation, are likely caused by a discrepancy between CPO formation of quartz and CPO formation of mica.
629 The samples are oriented according to their visible mineral stretching lineation, which was formed by
630 quartz in most samples. The alignment of high velocities is, however, caused mostly by mica CPO and
631 undulating mica grains around the stretching lineation. ~~The CPO of quartz and mica was not necessarily
632 formed at the same time and could represent different deformation stages.~~

633 The sample measured in the lab, RK15-22, similar to the case of the orthogneiss sample, shows a higher
634 influence of mica on AV_p due to its alignment in the foliation and similarly oriented microcracks. While in
635 the calculated V_p distribution, high velocities are distributed within the foliation plane, the measured
636 velocities show a distinct maximum in the lineation direction. The measured version also shows a higher
637 AV_p than the one calculated from the CPO. The difference, however, is not as large as for the orthogneiss
638 sample. In case of the paragneiss sample the measured AV_p is higher than the calculated one by a factor
639 of 1.5. Similar to the orthogneisses, this value is well in the range of ~~other literature published data~~
640 comparing experimental and modeled anisotropy ~~data~~. While experimental anisotropies are always higher
641 than the ones modeled using CPO, the factor is variable for gneiss samples ranging from 1.3 (e.g. Vasin et
642 al., 2017) to 6.6 (e.g. Ullemeyer et al., 2006). Considering experimental and modeled elastic anisotropy
643 data of 18 gneiss samples from different studies, experimental anisotropy is 3 times higher than the
644 modeled ones on average (Ivankina et al., 2005; 2017; Punturo et al., 2005; Ullemeyer et al., 2006; 2018;
645 Kern et al., 2008; Kern, 2009; Llana-Fúnez et al., 2009; Lokajicek et al., 2014; Zel et al., 2015; Vasin et al.,
646 2017). V_p/V_s ratios of the paragneisses are determined by the volume percentage of quartz and yield values
647 of 1.55-1.64. Higher volume percentages of quartz lead to lower V_p/V_s ratios.

648 Comparing the V_p velocities calculated from the Voigt model (Figure 5B) and the GMS crack free model
649 (Table 3) of the RK15-22 sample, it is evident that the Voigt model velocities are $\approx 300-400$ m/s higher. Yet,
650 symmetries of velocity distributions and AV_p coefficients computed using these two models are quite close,
651 suggesting that the Voigt modeling is reliable to assess the degree of elastic anisotropy of gneisses.

652 Tables 3 and 4 demonstrate a correlation of measured ultrasonic wave velocities and their anisotropy in
653 RK15-22 gneiss as well as the GMS model based on utilizing the two types of cracks ~~discussed earlier~~ at

654 pressures of 5-300 MPa as presented before. At 2 MPa, and also at atmospheric pressure, the proposed
655 model was not able to correctly reproduce experimental V_p patterns. At low confining pressure it is
656 observed that both self-consistent and non-interactive theories may be inadequate to describe the elastic
657 velocity behavior, which might beis mainly due to a lack of knowledge of unknown crack geometries
658 (Hadley, 1976). It is likely that another system of thinner microcracks is required to match the GMS model
659 and experimental ultrasonic wave velocities in RK15-22 at very low confining pressure-values.
660 As expected, the GMS models of RK15-22 at higher pressure require lower crack densities/porosities to
661 describe the experimental ultrasonic data. Modeling suggests that thinner type I cracks are closed at a
662 faster rate with increasing pressure compared to thicker type II cracks. Yet, due to an initially lower crack
663 density of type II cracks, the modeling suggests that their influence on the bulk elastic properties of model
664 RK15-22 gneiss becomes negligible at and above a pressure of 200 MPa. In contrast, type I cracks are
665 necessary to match the experimental and model P-wave velocities at a pressure of 300 MPa and we could
666 only roughly estimate that these cracks will be closed at a pressure of ≈ 740 MPa. To estimate the closing
667 pressure of type I cracks, we disregarded RK15-22 elastic anisotropy and calculated average Young's
668 modulus and Poisson ratio of the gneiss. According to the simple model of crack closure in the isotropic
669 rock (Walsh, 1965), the closing pressure of type I cracks is ≈ 740 MPa.
670 Naturally, the proposed model based on laboratory measurements of rock properties is quite simplistic,
671 with some limitation coming from the modelling method itself, and others related to available
672 experimental data. The GMS treats material as an infinite effective medium, which is filled by ellipsoidal
673 inclusions without gaps or overlaps. Local heterogeneities, stress concentrators arising, e.g., on grain
674 boundaries, correlations in grain positions or orientations, or size-related effects are not considered. For
675 the "average" rock, accessory phases were discarded, and the most characteristic ODFs, volume fractions
676 and grain shapes of main minerals were used assuming that the studied set of samples represents the
677 Adula Nappe sufficiently well. We assumed that microcrack systems and their closure with pressure in the
678 "average" rock is the same as in the paragneiss sample. A shape related distribution of microcracks,
679 deviations of the assumed SPOs of the cracks from those actually present in the gneiss, possible
680 dependence of microcrack SPO on shape of cracks, and changes of all these parameters with pressure,
681 including irreversible closure of different microcracks, are neglected. Our results suggest that even small
682 open crack densities at relatively high confining pressures have a notable influence on the elastic
683 anisotropy of the paragneiss. Therefore, a comprehensive and precise quantification of the microcrack
684 characteristics is necessary to simulate realistic models of pressure dependencies on the bulk elastic
685 properties of rocks. Naturally, the proposed model is quite simplistic, neglecting, e.g., the distribution of
686 microcracks with respect to shape, deviations of the assumed SPOs of the cracks from those actually
687 present in the gneiss, possible dependence of microcrack SPO on shape of cracks, and changes of all these
688 parameters with pressure. Our results suggest that even small open crack densities at relatively high
689 confining pressures have a notable influence on the elastic anisotropy of the paragneiss. Therefore, a
690 precise quantification of the microcrack characteristics is necessary to simulate realistic models of
691 pressure dependencies on the bulk elastic properties of rocks.

692

693 56.1.3. Marble

694

695 In the marble sample, the maximum V_p is at a ~~slight-small~~ angle to the lineation caused by the influence of
696 both the dolomite and the calcite CPO. The AV_p of marble in the literature is highly variable depending on
697 the grade of deformation (Burlini and Kunze, 1999; Zappone et al., 2000; Punturo et al., 2005; Schmidtkte
698 et al., ~~2021-in-prep~~). Since the marble lenses in the Adula Nappe only make up a few meters in thickness
699 they do not contribute to the overall elastic anisotropy of the unit ~~in any significant~~ to large amounts.
700 Depending on the thickness and distribution of such lenses or layers, they would have to ~~could be~~
701 considered for carbonate-rich crustal models. The sample yields a high V_p/V_s ratio of 1.82, which is
702 influenced by both calcite and dolomite. These high V_p/V_s ratios are typical for marble (e.g. Keppler et al.,
703 2015). The combination of high V_p/V_s ratio, as well as high AV_p , may constrain a very specific signal for
704 marble-rich crust at depth and help to detect specific features such as large subducted carbonate
705 platforms.

706

707 5.6.1.4. Metabasites

708

709 The AV_p of the metabasites is ~~determined-dominated~~ by hornblende, which has the highest volume
710 percentage and is the only mineral showing a strong CPO. Highest VP is found within the lineation and
711 caused by the alignment of (001), which is close to the highest VP in hornblende single crystals. Due to the
712 stronger hornblende CPO of RK15-4, the AV_p is higher in this sample. Studies on elastic anisotropies of
713 metabasites mainly focus on eclogites and blueschists (e.g. Abalos et al., ~~2010~~2011; Bezacier et al., 2010;
714 Keppler et al., 2017; Zertanti et al., 2019). Many of the metabasic units exhumed during continental
715 collision, however, are strongly retrogressed with large amounts of amphibole and/or chlorite. Recent
716 studies show that these retrogressed rocks frequently show higher elastic anisotropy than pristine basalts,
717 gabbros or also eclogites due to higher elastic anisotropy of amphiboles compared to pyroxenes, as well
718 as a pronounced deformation during exhumation (e.g. Neufeld et al., 2008; Keppler et al., 2016; Park and
719 Jung, 2020; Schmidtkte et al., ~~submitted to same issue~~2021). V_p/V_s ratios of 1.79 and 1.76 for RK15-4 and
720 RK15-7, respectively, are typical for metabasites (e.g. Worthington et al., 2013; Schmidtkte et al.,
721 ~~submitted to same issue~~2021).

722

723 5.6.2. Elastic anisotropy of the modeled “average” rock

724

725 Realistic upscaling of the rock elastic properties measured within limited scale or on laboratory samples
726 to the seismic scale is of a long-standing interest, e.g., in hydrocarbon reservoirs (Sayers, 1998; Bayuk et
727 al., 2008; Avseth et al., 2010). Here, we consider a rather homogeneous crystalline rock with low crack
728 porosity, and we try to build an effective large-scale model using features of the studied rock massif:
729 average mineral volume fractions, preferred orientations, grain shapes and microcracks systems.

730 As expected, the “average” rock shows a distribution of high V_p values normal to the Z-axis due to the
731 preferred orientation of mica, with a maximum V_p value at an angle to the X-axis due to the influence of
732 the preferred orientation of quartz (Fig. 7). This is a common pattern in the natural sample set (Fig. 5A
733 and B). Some orthogneisses in the natural sample set show maxima at an angle to the foliation normal,
734 which is different from the average sample (Fig. 5A). However, these samples generally show a low AV_p
735 and do not strongly contribute to the overall anisotropy. The model suggests decreasing AV_p and increasing
736 V_p values with increasing depth due to the closure of microcracks. A crack free “average” rock has V_p values

737 slightly over 6 km/s and a rather low AV_p of 4%, which is in between AV_p values characteristic for
738 paragneisses and orthogneisses. At lower confining pressure down to 5 MPa (corresponding to a depth of
739 ≈ 200 m), the model suggests a decrease of V_p values to ~ 4.5 km/s, and an increase of AV_p to 12% (Table
740 4) due to open microcracks.

741 ~~Some orthogneisses in the natural sample set show maxima at an angle to the foliation normal, which is~~
742 ~~different from the average sample (Fig. 5A). However, these samples generally show a low AV_p and do not~~
743 ~~strongly contribute to the overall anisotropy.~~

744 ~~What are the limitations of the proposed model? As discussed in 5.1.2, one of the main improvements~~
745 ~~of our model may be made by is the~~ better quantification of microcrack systems, as explained in section
746 6.1.2. Crack closure with increasing pressure in anisotropic gneisses should be studied in more detail to
747 reliably expand the crack closure in RK15-22 paragneiss to the large rock units massif in general. In addition
748 to crack closure due to pressure, microcracks in quartz grains may be sealed by solution-precipitation
749 processes (e.g. Brantley et al., 1990; Vollbrecht et al., 1991; Derez et al., 2015). Microfractures parallel to
750 the r- and z rhombohedral planes of quartz can heal after little or no shear displacement (e.g. Menegon et
751 al., 2008). These healed cracks frequently occur as fluid inclusions trails in quartz grains. Experimentally
752 deformed quartz showed that the trails are commonly arranged in planes parallel to the compression axis
753 (Stünitz et al., 2017). Some inclusion trails found in the current samples could be part of the same process
754 (APPENDIX - Fig. 2). Intragranular microcracks can also be crystallographically controlled (Vollbrecht et al.,
755 1999). Hence, when the CPO of quartz is strong, a preferred microcrack alignment can also be related to
756 certain crystallographic orientations.

757 Further model improvement may be achieved by more detailed constraints on the mineral volume
758 fractions and crystallographic textures within the rock massif via more extensive sampling.

759 The calculated “average” rock model is related to the XYZ coordinate frame, defined by rock foliation and
760 lineation. To improve the model, it is necessary to account for possible foliation or lineation direction
761 changes through the rock unit-massif by relating all crystal and shape preferred orientations to the same
762 global reference frame, e.g., geographical coordinates.

763 It is evident that the calculated model of the “average” rock does not consider large scale layering. It may
764 be introduced into the model by creating “average” rock layers consisting of the characteristic minerals
765 with their preferred orientations and microstructures and using a Backus averaging to combine thin
766 (relative to the lateral size) rock layers into a seismic scale effective medium (Backus, 1962; Sayers, 1998).
767 Furthermore, large scale faults are an important factor when considering elastic anisotropy and have to
768 be considered in any model of the Alps. Finally, only confining pressures and the density of the crack-free
769 “average” rock were used to estimate the depth values. Compositional variations would change the depth
770 estimates.

771 Despite all these simplifications of the current model, in principle, the proposed “average” rock may be
772 constructed to represent effective elastic properties on any necessary scale if there is sufficient
773 information on modal composition, textures and microstructures available from the selected samples. ~~It~~
774 ~~would be interesting to make a~~ Then direct comparison of the “average” rock with seismic data on the
775 uppermost layer of the crust can be made.

776

777

778 5.3. Elastic anisotropy in the Alps

779
780 The well-studied geology of the Alps provides comprehensive foliation and lineation maps (e.g., Steck
781 1990). Surface data can be correlated with seismic imaging making it possible to construct models for
782 different tectonic structures at depth (e.g. Yosefnejad et al., 2017). For the present study, the Adula Nappe
783 was chosen as a representative unit for deformed ~~upper~~ crust in the Alps. The central part of the Adula
784 Nappe, where the samples for this study have been collected exhibits a shallowly NE dipping foliation and
785 a NS trending lineation mainly formed during peak pressure and early stages of exhumation. ~~P~~ The
786 northern and southern parts of the nappe ~~further to the north as well as the south~~, however, have been
787 overprinted by younger deformation (e.g. Löw, 1987; Nagel, 2008; Kossak et al. 2017).

788 The afore mentioned discrepancy between quartz lineation and mica CPO in several of the samples has
789 not ~~well~~ been well studied with respect to the seismic anisotropy. It could be a common issue for most
790 upper crustal units in the Alps, exhibiting a complicated deformation history. Hence, maxima for elastic
791 anisotropies in the lineation direction in mica rich rocks cannot simply be correlated to measurements in
792 the field.

793 Microcrack distribution and orientation have not been investigated systematically throughout the rock
794 units of the Alps and they might exhibit strong local variations corresponding to the large-scale fracture
795 and fault pattern (e.g. Vilhelm et al., 2010). This has also a great effect on the travel times of P- and S-
796 waves, i.e. V_P and V_S are significantly decreased (e.g. Yan et al., 2005; Kelly et al., 2017) and therefore
797 needs to be considered for any large-scale section or model of the Alps (e.g. TRANSALP: Lüschen et al.,
798 2004; Millahn et al., 2005; AlpArray: Hetényi et al., 2018; Molinari et al., 2020).

799 While deformed granitoids (e.g. orthogneisses) and deformed clastic metasediments (e.g. paragneisses)
800 are the dominant lithologies, the rock spectrum found in the Alps and other collisional orogens ranges
801 from sedimentary rocks as well as metasediments like marbles, micaschists and quartzites, over
802 metabasites like eclogites, blueschists, amphibolites and greenschists to ultrabasic rocks like peridotites
803 and serpentinites. These lithologies might occur as small layers within the larger gneiss massifs
804 contributing to the overall seismic properties, but they also occur throughout the Alps as large coherent
805 units, which have to be considered. Furthermore, volcanic and plutonic intrusions are a common
806 occurrence in collisional orogens.

807 There are several nappes within the Alps dominated by (meta-)basic (e.g. the Zermatt–Saas zone:
808 Angiboust et al., 2009) and ultrabasic rocks (e.g. the Ivrea Complex: Hartmann and Wedepohl, 1993), which
809 have to be considered in some seismic profiles across the Alps. While we present data on some common
810 minor lithologies, like amphibolite, marble and micaschist, we also refer the reader to data on
811 metasediments (e.g. Punturo et al., 2005), metabasites (e.g. Abalos et al., 2011; Bezacier et al., 2010;
812 Zertani et al., 2020; Schmidtke et al., ~~submitted to same issue~~2021) and ultrabasic rocks (Mainprice et al.
813 2000; Ullemeyer et al., 2010). Within the NFP20 EAST profile considered in the present study, amphibolites
814 and marbles mostly occur as small lenses of under 1 km of thickness ~~and are likely not detectable with~~
815 ~~seismic imaging at depth.~~ Detecting them within the bulk of paragneisses and orthogneisses is less likely.
816 If they produce a seismic anisotropy signal will depend, of course, on the seismic wave length. Zertani et
817 al. (2020), for example, used the finite element method to employ eclogite facies shear zones within
818 granulites in models for petrophysical properties. ~~The~~ In the present work, however, we consider the
819 elastic anisotropy of major gneiss units is therefore most decisive-critical for the investigated part of the
820 section and other rock units are negligible because of their small volume proportion. Therefore smaller

821 lithological variations as well as geometrical irregularities have been ignored for the overall model. Gneiss
822 samples in this as well as previous studies generally show an alignment of high V_P within the foliation plane.
823 That is why the foliation of gneisses and mica schists formed during continental collision and exhumation
824 is likely a main factor controlling the elastic anisotropies of the continental crust in collisional orogens. The
825 data presented in this study yield a first approximation for average ~~upper~~ crustal seismic properties with
826 increasing depth as well as the specific seismic property spectrum of this deformed upper crustal section
827 of the Alps.

828
829

830 6.7. Summary and Conclusion

831

832 1. The investigation of a large set of rocks collected in the Adula Nappe, which is considered to be
833 representative of deformed upper crustal rocks in the Alps, indicates a large variety of elastic anisotropies.

834

835 2. The Adula Nappe is mostly made up of orthogneisses with modelled AVP between 1.3 and 5.3% and
836 V_P/V_S ratios between 1.51 and 1.67, as well as paragneisses with modelled AVP between 2.0% to 20.5%
837 and V_P/V_S ratios between 1.55 and 1.645.

838

839 3. ~~Small lenses of less than 100 m thick m~~Metabasites that make up only 100 m thick lenses, show an AVP
840 of 2-4.5% and V_P/V_S ratios of 1.76-1.79. Marble lenses of even smaller dimensions yield an AVP of 3.4%
841 and V_P/V_S ratio of 1.83. Yet, these lenses are statistically ~~insignificant of small significance~~ for the
842 considered section of para- and orthogneisses.

843

844 4. Orthogneiss and paragneiss measured in the lab using ultrasound both show higher AVP as well as lower
845 V_P compared to the ones modelled using CPO, which is caused by open microcracks in the rocks at shallow
846 depth.

847

848 5. Average elastic anisotropies were calculated for a typical gneiss using common CPO types of constituent
849 mineral phases, mineral content, grain shapes and crack systems within the sample set. Calculated elastic
850 constants are considered to be representative for the range of depths from a few hundred meters up to
851 ≈ 28 km. The modelled "average" gneiss yields an AV_P of 4% at a depth of ≈ 28 km, where the vast majority
852 of microcracks is closed. Due to the opening of microcracks, the elastic anisotropy of the model gneiss
853 increases towards shallower depth and reaches $AV_P = 12\%$ at ≈ 0.2 km. This makes it possible to either
854 choose parameters of an average sample representative of rocks at depths higher than 28 km, or choose
855 an average sample at increasingly lower depth with progressively opening microcracks, depending on the
856 depth of interest.

857

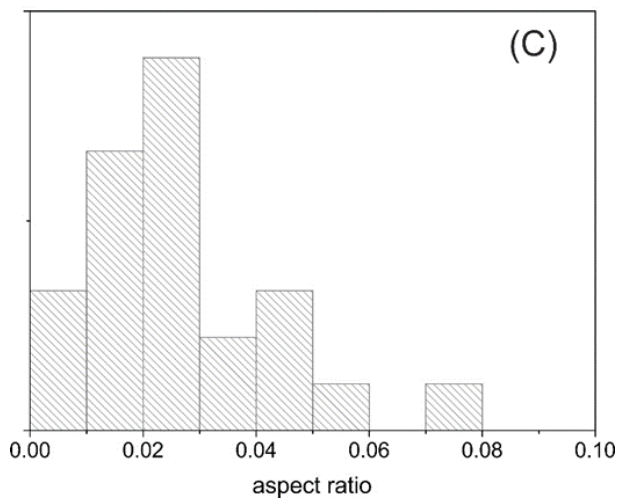
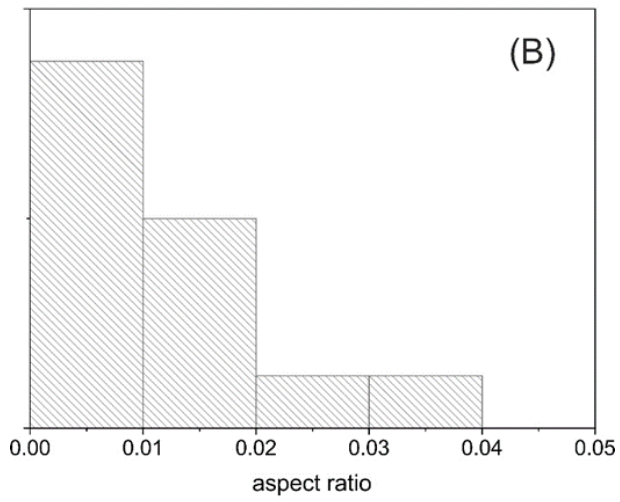
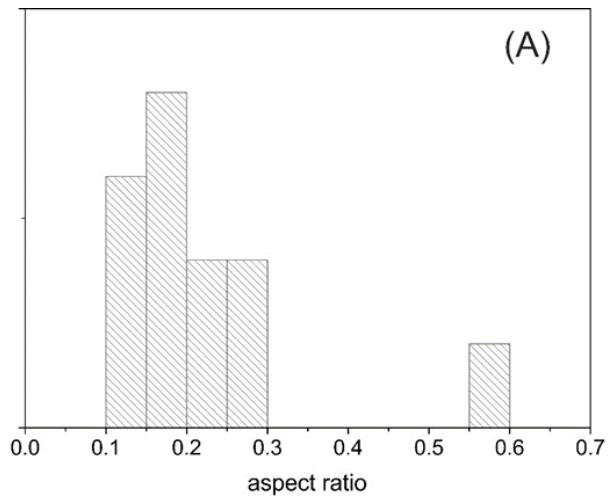
858

859 Acknowledgement

860

861 We are grateful for the very constructive and elaborate reviews by Benito Abalos, Sascha Zertani, as well
862 as the anonymous reviewer. These reviews strongly improved our manuscript. This study was funded by

863 the German research foundation (DFG-grant No. KE 2268/2-1, STI298/9-1) as part of the DFG priority
864 programme “Mountain Building Processes in 4 Dimensions”. Fruitful discussions within the priority
865 programme are gratefully acknowledged. Furthermore, this study was partially supported by the Czech
866 Science Foundation research grants 18-08826S, 21-26542S and by the Czech Academy of Sciences project
867 RVO 67985831. Authors appreciate the access to the SKAT diffractometer at FLNP JINR. The project was
868 partially supported by the JINR theme No. 04-4-1121-2015/2020.
869



872 APPENDIX - Figure 1: Distributions of aspect ratios of mica grains (A), type I (B) and type II (C) cracks based
 873 on analysis of several RK15-22 thin sections.



874
 875 APPENDIX – Figure 2: Grains of quartz crossed by type II cracks, XZ plane. Parallel to them are some
 876 inclusion trails, which could be former microcracks sealed by solution precipitation. White scale bar is 0.4
 877 mm.

<u>Orthogneiss</u>	<u>quartz C-axes</u>	<u>Paragneiss</u>	<u>quartz C-axes</u>
<u>GAN12</u>	<u>periphery</u>	<u>GAN08</u>	<u>periphery</u>
<u>JK6</u>	<u>periphery</u>	<u>GAN15</u>	<u>between Z and Y</u>
<u>MS17-15</u>	<u>between Z and Y</u>	<u>MS17-12B</u>	<u>between Z and Y</u>
<u>RK15-9A</u>	<u>periphery</u>	<u>MS17-12C</u>	<u>between Z and Y</u>
<u>RK15-9B</u>	<u>periphery</u>	<u>RK15-5</u>	<u>between Z and Y</u>
<u>RK15-10</u>	<u>periphery</u>	<u>RK15-18</u>	<u>between Z and Y</u>
<u>RK15-11A</u>	<u>between Z and Y</u>	<u>RK15-22</u>	<u>between Z and Y</u>
<u>RK15-17</u>	<u>between Z and Y</u>	<u>RK60</u>	<u>between Z and Y</u>
<u>RK15-20</u>	<u>periphery</u>	<u>RK70A</u>	<u>between Z and Y</u>
<u>RK15-24B</u>	<u>between Z and Y</u>	<u>SADU16</u>	<u>between Z and Y</u>
<u>RK15-27B</u>	<u>periphery</u>	<u>SADU30</u>	<u>periphery</u>
<u>RK15-28</u>	<u>between Z and Y</u>	<u>ZAP01</u>	<u>periphery</u>
<u>RK15-30B</u>	<u>between Z and Y</u>		
<u>RK15-31</u>	<u>periphery</u>		
<u>RK63B</u>	<u>between Z and Y</u>		
<u>RK66</u>	<u>girdle</u>		
<u>SADU39</u>	<u>periphery</u>		

878
 879 APPENDIX – Table 1: CPO patterns of quartz C-axes maxima within the sample set.

880 REFERENCES:

881

882 Ábalos, B., D. M. Fountain, J. I. Gil Ibarguchi, and P. Puelles: Eclogite as a seismic marker in subduction
883 channels: Seismic velocities, anisotropy, and petrofabric of Cabo Ortegal eclogite tectonite (Spain), *Geol.*
884 *Soc. Am. Bull.*, 123, 439–456, 2011.

885

886 Abrecht, J.: Geologic units of the Aar massif and their pre-Alpine rock associations: a critical review,
887 *Schweiz. Mineral. Petrogr. Mitt.*, 74, 5-27, 1994.

888

889 Aleksandrov, K.S., Alchikov, U.V., Belikov, B.P., Zaslavski, B.I., and Krupny, A.I.: Elastic wave velocities in
890 minerals at atmospheric pressure and increasing precision of elastic constants by means of EVM, *Izvestija*
891 *Academy of Science USSR, Geol. Ser.* 10, 15–24, 1974.

892

893 Aleksandrov, K.S., and Ryzhova, T.V.: The elastic properties of rock forming minerals, *Izvestija Academy of*
894 *Science USSR, Geophys. Ser.* 12, 1799–1804, 1961.

895

896 Almqvist, B. S.G., Hirt, A. M., Herwegh, M., Ebert, A., Walter, J. M.; Leiss, B., Burlini, L.: Seismic anisotropy
897 in the Morcles nappe shear zone: Implications for seismic imaging of crustal scale shear zones,
898 *Tectonophysics*, 603, pp. 162-178, 2013.

899

900 Almqvist, B. S.G., and Mainprice, D.: Seismic properties and anisotropy of the continental crust: Predictions
901 based on mineral texture and rock microstructure, *Reviews of Geophysics*, 55, pp. 367-433, 2017.

902

903 Angiboust S., Agard P., Jolivet L. and Beyssac O.: The Zermatt-Saas ophiolite: the largest (60-km wide) and
904 deepest (c. 70–80 km) continuous slice of oceanic lithosphere detached from a subduction zone? *Terra*
905 *Nova* 21, 171–180, 2009.

906

907 Avseth, P., Mukerji, T., Mavko, G., and Dvorkin, J.: Rock-physics diagnostics of depositional texture,
908 diagenetic alterations, and reservoir heterogeneity in high-porosity siliciclastic sediments and rocks — A
909 review of selected models and suggested work flows, *Geophysics*, 75(5), 75A31-75A47, 2010.

910

911 Babuška, V. (1968). Elastic anisotropy of igneous and metamorphic rocks. *Studia Geophysica et*
912 *Geodaetica*, 12(3), 291-303. <https://doi.org/10.1007/BF02592385>

913

914 [Backus, G. E.: Long-wave elastic anisotropy produced by horizontal layering, *Journal of Geophysical*](#)
915 [Research](#), 67, 11, 4427–4440, 1962.

916

917 Barruol, G., Bonnin, M., Pedersen, H. Bokelmann, G.H.R. and Tiberi, C.: Belt-parallel mantle flow beneath
918 a halted continental collision: The Western Alps, *Earth and Planetary Science Letters*, 302, 3–4, 429-438,
919 2011.

920

921 Barruol, G., Deschamps, A. and Coutant, O.: Mapping upper mantle anisotropy beneath SE France by SKS
922 splitting indicates Neogene asthenospheric flow induced by Apenninic slab roll-back and deflected by the
923 deep Alpine roots, *Tectonophysics*, 394, 1–2, 125-138, 2004.

924

925 Barruol, G., and Kern, H.: Seismic anisotropy and shear-wave splitting in lower-crustal and upper-mantle
926 rocks from the Ivrea Zone—Experimental and calculated data, *Phys. Earth Planet. Inter.* 95, 3-4, 175–194,
927 1996.

928

929 Bascou, J., G. Barruol, A. Vauchez, D. Mainprice, and M. Eglydio-Silva: EBSD-measured lattice-preferred
930 orientations and seismic properties of eclogites, *Tectonophysics*, 342, 61–80, 2001.

931

932 Bayuk, I.O., Ammerman, M., and Chesnokov, E.M.: Upscaling of elastic properties of anisotropic
933 sedimentary rocks, *Geophys. J. Int.*, 172, 842-860, 2008.

934

935 Ben Ismail, W. and D. Mainprice: An olivine fabric database: an overview of upper mantle fabrics and
936 seismic anisotropy, *Tectonophysics*, 296, 145-157, 1998.

937

938 Berryman, J.G.: Long-wavelength propagation in composite elastic media I. Spherical inclusions, *Journal of*
939 *Acoustical Society of America*, 68, 1809-1819, 1980.

940

941 Bezacier, L., Reynard, B., Bass, J.D., Wang, J., and Mainprice, D.: Elasticity of glaucophane, seismic velocities
942 and anisotropy of the subducted oceanic crust, *Tectonophysics* 494, 201–210, 2010.

943

944 Bhagat, S.S., Bass, J.D., Smyth, and J.R.: Single-crystal elastic properties of omphacite-C2/C by Brillouin
945 spectroscopy, *J. Geophys. Res. Solid Earth* 97, 6843–6848, 1992.

946 [Bokelmann, G. H. R., Qorbani, E., and Bianchi, I.: Seismic anisotropy and large-scale deformation of the](#)
947 [Eastern Alps, *Earth and Planetary Science Letters*, 383, 1–6, 2013.](#)

948

949 [Brantley, S.L., Brantley, B. Evans, S.H., Hickman, D.A. Crerar: Healing of microcracks in quartz: Implications](#)
950 [for fluid flow. *Geology* 18, 136–139, 1990.](#)

951

952 Brown, J.M., Abramson, E.H., and Angel, R.J: Triclinic elastic constants for low albite, *Phys. Chem. Miner.*
953 33, 256–265, 2006.

954

955 Burlini, L., and Kunze, K.: Fabric and Seismic Properties of Carrara Marble Mylonite, *Phys. Chem. Earth*, 25,
956 2, 133-139, 2000.

957

958 Challandes, N., Marquer, D., and Villa, I.M.: P-T-t modelling, fluid circulation, and ³⁹Ar-⁴⁰Ar and Rb-Sr mica
959 ages in the Aar Massif shear zones (Swiss Alps), *Swiss J. Geosci.*, 101, 269-288, 2008.

960

961 [Christensen, N.I.: Compressional wave velocities in metamorphic rocks at pressures to 10 kbar. *Journal of*](#)
962 [Geophysical Research](#), 70, 6147-6164, 1965.

963
964 [Christensen, N. I.: Compressional wave velocities in rocks at high temperatures and pressures, critical](#)
965 [thermal gradients, and crustal low-velocity zones. Journal of Geophysical Research: Solid Earth, 84\(B12\),](#)
966 [6849–6857, 1979.](#)
967
968 Christensen, N.I. Compressional wave velocities in possible mantle rocks to pressures of 30 kilobars, J.
969 Geophys. Res., 79_(2), 407-412, 1974.
970
971 [Cholach, P.Y., and Schmitt, D.R.: Intrinsic elasticity of a textured transversely isotropic muscovite](#)
972 [aggregate: Comparisons to the seismic anisotropy of schists and shales. Journal of Geophysical Research,](#)
973 [111, B09410, 2006.](#)
974
975 [Christensen, N.I. and Mooney, W.D.: Seismic velocity structure and composition of the continental crust:](#)
976 [a global view. Jour. Geophys. Res., 100 B7: 9761-9788, 1995.](#)
977
978 Christoffel, E.B.: Über die Fortpflanzung von Stößen durch elastische, feste Körper, Annali di Matematica
979 8, 193–243, 1877.
980
981 Dale, J., Holland, T.B.J.: Geothermobarometry, P–T paths and metamorphic field gradients of high-pressure
982 rocks from the Adula Nappe, Central Alps. Journal of metamorphic Geology, 21, 813-829, 2003.
983
984 Dandekar, D.P.: Variation in the elastic constants of calcite with pressure, Am. Geophys. Union Trans. 49,
985 323 pp., 1968.
986
987 [Derez, T., Pennock, G., Drury, M. and Sintubin, M.: Low-temperature intracrystalline deformation](#)
988 [microstructures in quartz. Journal of Structural Geology, 71, 3-23, 2015.](#)
989
990 [Engi, M., Todd, S.C. and Schmatz, D.R.: Tertiary metamorphic conditions in the eastern Lepontine Alps.](#)
991 [Schweizerische Mineralogische und Petrographische Mitteilungen, 75, 347–396, 1995.](#)
992
993 Erdman, M. E., Hacker, B.R., Zandt, G., and Seward, G.: Seismic anisotropy of the crust: Electron-
994 backscatter diffraction measurements from the Basin and Range, Geophys. J. Int., doi:10.1093/gji/ggt287,
995 2013.
996
997 [Faccenda, M., Ferreira, A. M. G., Tisato, N., Lithgow-Bertelloni, C., Stixrude, L., & Pennacchioni, G.: Extrinsic](#)
998 [Elastic Anisotropy in a Compositionally Heterogeneous Earth's Mantle, Journal of Geophysical Research:](#)
999 [Solid Earth, 124, 1671-1687, 2019.](#)
1000
1001 [Froitzheim, N., and Manatschal, G.: Kinematics of Jurassic rifting, mantle exhumation, and passive-margin](#)
1002 [formation in the Austroalpine and Penninic nappes \(eastern Switzerland\), Geological Society of America](#)
1003 [Bulletin, 108, 9, 1120–1133, 1996.](#)
1004

1005 Fry, B., Deschamps, F., Kissling, E., Stehly, L., and Giardini, D.: Layered azimuthal anisotropy of Rayleigh
1006 wave phase velocities in the European Alpine lithosphere inferred from ambient noise, *Earth Planet. Sci.*
1007 *Lett.*, 297, 1–2, 95-102, 2010.

1008

1009 Goncalves, P., Olliot, E., Marquer, D., and Connolly, J.: Role of chemical processes on shear zone formation:
1010 an example from the Grimsel metagranodiorite (Aar massif, Central Alps), *Journal of Metamorphic*
1011 *Geology*. 30. 10.1111/j.1525-1314.2012.00991.x, 2012.

1012

1013 Hadley, K.: Comparison of calculated and observed crack densities and seismic velocities in Westerly
1014 granite. *J. Geophys. Res.*, 81(20), 3484-3494, 1976.

1015

1016 Hartmann G. and Wedepohl K.H.: The composition of peridotite tectonites from the Ivrea Complex,
1017 northern Italy: Residues from melt extraction. *Geochim. Cosmochim. Ac.*, 57, 1761-1782, 1993.

1018

1019 Heinrich, C. A.: Eclogite facies regional metamorphism of hydrous mafic rocks in the Central
1020 Alpine Adula nappe. *J. Petrol.*, 27, 123–154, 1986.

1021

1022 [Hetényi G., I. Molinari, J.-Clinton, J., Bokelmann, G., Bondár, I., Crawford, W. C., Dessa, J.-X., Doubre, C.,](#)
1023 [Friederich, W., Fuchs, F. et al.: The AlpArray Seismic Network: a large-scale European experiment to image](#)
1024 [the Alpine orogeny. *Surveys in Geophysics*, 39, 1009-1033, 2018.](#)

1025

1026 Hetényi, G. Plomerová, J. Bianchi, I. Kampfová Exnerová, H. Bokelmann, G., Handy, M.R., and Babuška, V.:
1027 From mountain summits to roots: crustal structure of the Eastern Alps and Bohemian Massif along
1028 longitude 13.3° E, *Tectonophysics*, 744, 239-255, 2018.

1029

1030 Heyliger, P., Ledbetter, H., Kim, S.: Elastic constants of natural quartz, *J. Acoust. Soc. Am.* 114, 644–650,
1031 2003.

1032

1033 Huang, J., Devoe, M., Gomez-Barreiro, J., Ren, Y., Vasin, R., Wenk, H.-R.: Preferred orientation and
1034 anisotropy of Slates from Northern Spain. *International Journal of Earth Sciences*, 2021. (submitted)

1035

1036 Humbert, P., and Plique, F.: Propriétés élastiques de carbonates rhomboédriques monocristallins calcite,
1037 magnésite, dolomite, *C.R. Acad. Sci. Paris*, 275, 391–394, 1972.

1038

1039 Ivankina, T.I., Kern, H., and Nikitin, A.N.: Directional dependence of P- and S-wave propagation and
1040 polarization in foliated rocks from the Kola superdeep well: evidence from laboratory measurements and
1041 calculations based on TOF neutron diffraction, *Tectonophysics* 407, 25–42, 2005.

1042

1043 Ivankina, T.I., Zel, I.Yu., Lokajicek, T., Kern, H., Lobanov, K.V., and Zharikov, A.V.: Elastic anisotropy of
1044 layered rocks: ultrasonic measurements of plagioclase-biotite-muscovite (sillimanite) gneiss versus
1045 texture-based theoretical predictions (effective media modeling), *Tectonophysics*
1046 DOI:10.1016/j.tecto.2017.05.005, 2017.

1047 [Ji, S., and Salisbury, M.H.: Shear-wave velocities, anisotropy and splitting in high-grade mylonites.](#)
1048 [Tectonophysics, 221, 453-473, 1993.](#)

1049

1050 [Ji, S., Salisbury, M.H. and Hanmer, S.: Petrofabric, P-wave anisotropy and seismic reflectivity of highgrade](#)
1051 [mylonites. Tectonophysics, 222: 195-226, 1993.](#)

1052

1053 [Ji, S., Wang, Q. and Xia, B.: P-wave velocities of polymineralic rocks: comparison of theory and experiment](#)
1054 [and test of elastic mixture rules. Tectonophysics, 366, 165-185, 2003.](#)

1055

1056 Kachanov, M., and Mishakin, V.V.: On crack density, crack porosity, and the possibility to interrelate them,
1057 International Journal of Engineering Science, 142, 185-189, 2019.

1058

1059 [Karato, S., Jung, H., Katayama, I. and Skemer, P.: Geodynamic Significance of Seismic Anisotropy of the](#)
1060 [Upper Mantle: New Insights from Laboratory Studies, Annual Review of Earth and Planetary Science, 36,](#)
1061 [59-95, 2008.](#)

1062

1063 Kelly, C. M., D. R. Faulkner, and A. Rietbrock: Seismically invisible fault zones: Laboratory insights into
1064 imaging faults in anisotropic rocks, Geophys. Res. Lett., 44, 8205–8212, 2017.

1065

1066 Keppler, R., Behrmann, J.H., Stipp, M.: Textures of eclogites and blueschists from Syros island, Greece:
1067 inferences for elastic anisotropy of subducted oceanic crust, Geophys. Res. Solid Earth
1068 DOI:10.1002/2017JB014181, 2017.

1069

1070 [Keppler, R., Stipp, M., Behrmann, J.H., Ullemeyer, K., and Heidelbach, F.: Deformation inside a](#)
1071 [paleosubduction channel—insights from microstructures and crystallographic preferred orientations of](#)
1072 [eclogites and metasediments from the Tauern Window, Austria, J. Struct. Geol. 82, 60–79, 2016.](#)

1073

1074 Keppler, R., K. Ullemeyer, J. H. Behrmann, and M. Stipp: Potential of full pattern fit methods for the texture
1075 analysis of geological materials: Implications from texture measurements at the recently upgraded
1076 neutron time-of-flight diffractometer SKAT, J. Appl. Crystallogr., 47, 1520–1535, 2014.

1077

1078 Keppler, R., K. Ullemeyer, J. H. Behrmann, M. Stipp, R. Kurzwaski, and T. Lokajíček: Crystallographic
1079 preferred orientations of exhumed subduction channel rocks from the Eclogite zone of the Tauern Window
1080 (eastern Alps, Austria), and implications on rock elastic anisotropies at great depths, Tectonophysics, 647,
1081 89–104, 2015.

1082

1083 Kern, H., Ivankina, T.I., Nikitin, A.N., Lokajicek, T., and Pros, Z.: The effect of oriented microcracks and
1084 crystallographic and shape preferred orientation on bulk elastic anisotropy of a foliated biotite gneiss from
1085 Outokumpu, Tectonophysics 457, 143–149, 2008.

1086

1087 Kern, H., & Wenk, H.-R. (1990). Fabric-related velocity anisotropy and shear wave splitting in rocks from
1088 the Santa Rosa mylonite zone, California. *Journal of Geophysical Research*, 95, 11213–11223.
1089 <https://doi.org/10.1029/JB095iB07p11213>
1090
1091 Kitamura, K.: Constraint of lattice-preferred orientation (LPO) on Vp anisotropy of amphibole-rich rocks,
1092 *Geophys. J. Intern.* 165, 3, 1058-1065, 2006.
1093
1094 Kossak-Glowczewski, J., Froitzheim, N., Nagel, T.J., Pleuger, J., Keppler, R., Leiss, B., Regent, V.: Along-strike
1095 shear-sense reversal in the Vals-Scaradra Shear Zone at the front of the Adula Nappe (Central Alps,
1096 Switzerland). *Swiss Journal of Geosciences*, 110, 677-697, 2017.
1097
1098 [Kurz, W., Fritz, H., Tenczer, V. and Unzog, W.: Tectonometamorphic evolution of the Koralm Complex](#)
1099 [\(Eastern Alps\): constraints from microstructures and textures of the 'Plattengneis' shear zone. *Journal of*](#)
1100 [Structural Geology](#) 24, 1957-1970, 2002.
1101
1102 Laubscher, H.P.: Large-scale, thin-skinned thrusting in the southern Alps: Kinematic models, *GSA Bull.* 96,
1103 710-718, 1985.
1104
1105 [Lespinasse, M. and A. Pêcher: Microfracturing and regional stress field: a study of the preferred](#)
1106 [orientations of fluid inclusion planes in a granite from the Massif Central, France. *J. Struct. Geol.* 8, 169-](#)
1107 [180, 1986.](#)
1108
1109 [Link, F. and Rumpker, G.: Resolving seismic anisotropy in the lithosphere-asthenosphere in the](#)
1110 [Central/Eastern Alps beneath the dense SWATH-D network, *Front. Earth Sci.*, provisionally accepted, 2021,](#)
1111 [doi: 10.3389/feart.2021.679887.](#)
1112
1113 Llana-Fúnez, S., and Brown, D.: Contribution of crystallographic preferred orientation to seismic anisotropy
1114 across a surface analog of the continental Moho at Cabo Ortegal, Spain. *GSA Bull.* 124, 9/10, 1495–1513,
1115 2012.
1116
1117 Llana-Fúnez, S., Brown, D., Carbonell, R., Álvarez-Marrón, J., and Salisbury, M.: Seismic anisotropy of upper
1118 mantle-lower continental crust rocks in Cabo Ortegal (NW Spain) from crystallographic preferred
1119 orientation (CPO) patterns, *Trabajos de Geología, Universidad de Oviedo*, 29, 432-436, 2009.
1120
1121 Lokajicek, T., Kern, H., Svitek, T., and Ivankina, T.: 3D velocity distribution of P- and S-waves in a biotite
1122 gneiss, measured in oil as the pressure medium: Comparison with velocity measurements in a multi-anvil
1123 pressure apparatus and with texture-based calculated data, *Phys. Earth Planet. Inter.*, 231, 1-15, 2014.
1124
1125 Lokajíček, T., Vasin, R., Svitek, T., Petružálek, M., Kotrlý, M., Turková, I., Onysko, R., Wenk, H.R.: Intrinsic
1126 elastic anisotropy of Westerly granite observed by ultrasound measurements, microstructural
1127 investigations, and neutron diffraction, *J. Geophys. Res. Solid Earth*, 126, e2020JB020878, 2021.
1128

1129 Löw, S.: Die tektono-metamorphe Entwicklung der Nördlichen Adula-Decke. Beiträge zur Geologischen
1130 Karte der Schweiz N.F., 161, 1–84, 1987.
1131
1132 Lüschen, E., B. Lammerer, H. Gebrande, K. Millahn, and TRANSALP Working Group: Orogenic structure of
1133 the Eastern Alps, Europe, from TRANSALP deep seismic reflection profiling, *Tectonophys.*, 388 (1-4), 85-
1134 102, 2004.
1135
1136 Lutterotti, L., Matthies, S., Wenk, H.-R., Schultz, A.J., and Richardson, J.W.: Combined texture and structure
1137 analysis of deformed limestone from time-of-flight neutron diffraction spectra, *J. Appl. Phys.* 81, 594–600,
1138 1997.
1139
1140 Mainprice, D., Barruol, G. and Ben Ismail, W.: The seismic anisotropy of the Earth's mantle: from single
1141 crystal to polycrystal. In: Karato, S.-I., Forte, A.M., Liebermann, R.C., Masters, G., Stixrude, L. (Eds.), *Earth's
1142 deep interior: mineral physics and seismic tomography: from atomic to global: AGU Geophysics
1143 Monograph*, 237–264, 2000.
1144
1145 Mainprice, D., and Humbert, M.: Methods of calculating petrophysical properties from lattice preferred
1146 orientation data, *Surv. Geophys.* 15, 575–592, 1994.
1147
1148 Matthies, S.: On the combination of self-consistent and geometric mean elements for the calculation of
1149 the elastic properties of textured multi-phase samples, *Solid State Phenom.*, 160, 87–93, 2010.
1150
1151 Matthies, S.: GEO-MIX-SELF calculations of the elastic properties of a textured graphite sample at different
1152 hydrostatic pressures, *J. appl. Crystallogr.*, 45, 1–16, 2012.
1153
1154 Matthies, S., and Humbert, M.: On the principle of a geometric mean of even-rank symmetric tensors for
1155 textured polycrystals, *J. Appl. Crystallogr.* 28, 254–266, 1995.
1156
1157 Matthies, S., Lutteroti, and L., Wenk, H.R.: Advances in Texture Analysis from Diffraction Spectra, *J. Appl.
1158 Cryst.* 30, 31–42, 1997.
1159
1160 Matthies, S., and Wenk, H.-R.: Transformations for monoclinic crystal symmetry in texture analysis, *J. Appl.
1161 Cryst.*, 42, 564-571, 2009.
1162
1163 Mauler, A., L. Burlini, K. Kunze, P. Philippot, and J.-P. Burg: P-wave anisotropy in eclogites and relationship
1164 to the omphacite crystallographic fabric, *Phys. Chem. Earth*, 15, 119–126, 2000.
1165
1166 [Menegon, L., Pennacchioni, G., Heilbronner, R., Pittarello, L.: Evolution of quartz microstructure and c-axis
1167 crystallographic preferred orientation within ductilely deformed granitoids \(Arolla unit, Western Alps\).
1168 *Journal of Structural Geology* 30\(11\), 1332-1347, 2008.](#)
1169
1170 Meyre, C., and Pusching, A. R.: High-pressure metamorphism and deformation at Trescolmen,

1171 Adula nappe, Central Alps. Schweizerische Mineralogische und Petrographische Mitteilungen, 73,
1172 277–283, 1993.

1173

1174 Meyre, C., De Capitani, C., and Partsch, J. H.: A ternary solid solution model for omphacite and its
1175 application to geothermobarometry of eclogites from the Middle Adula nappe (Central Alps, Switzerland).
1176 Journal of Metamorphic Geology, 15, 687–700, 1997.

1177

1178 Millahn, K., Lüschen, E., Gebrande, H., and TRANSALP Working Group: TRANSALP-cross-line recording
1179 during the seismic reflection transect in the Eastern Alps. Tectonophys., 414, 39–49, 2005.

1180

1181 Molinari I., Obermann A., Kissling E., Hetényi G., Boschi L., and AlpArray-EASI working group: 3D crustal
1182 structure of the Eastern Alpine region from ambient noise tomography, Results in Geophysical Sciences,
1183 1–4, DOI: 10.1016/j.ringps.2020.100006, 2020.

1184

1185 [Montagner, J.-P., and Guillot, L.: Seismic Anisotropy and global geodynamics. Mineralogical Society of](#)
1186 [America, 51, 353-385, 2003.](#)

1187

1188 Morris, P.R. Elastic constants of polycrystals, Int. J. Eng. Sci., 8,49–61, 1970.

1189

1190 Nagel, T.J.: Subduction, collision and exhumation recorded in the Adula nappe, central Alps. In:
1191 Siegesmund, S., Fügenschuh, B., Froitheim, N. (Eds.), Tectonic Aspects of the Alpine–Dinarides–
1192 Carpathian System: Geological Society, London, Special Publications, 298, 365–392, 2008.

1193

1194 Nagel, T., De Capitani C. and Frey, M.: Isograds and P-T evolution in the eastern Lepontine Alps
1195 (Graubunden, Switzerland). Journal of Metamorphic Geology 20, 309-324, 2002.

1196

1197 [Neufeld, K., Ring, U., Heidelbach, F., Dietrich, S., and Neuser, R.D.: Omphacite textures in eclogites of the](#)
1198 [Tauern Window: Implications for the exhumation of the Eclogite Zone, Eastern Alps. Journal of Structural](#)
1199 [Geology, 30, 976–992, 2008.](#)

1200

1201 Nishizawa, O. and Yoshino, T.: Seismic velocity anisotropy in mica-rich rocks: an inclusion model,
1202 Geophysical Journal International 145, 19-32, 2001.

1203

1204 [Okaya, D., Vel, S. S., Song, W. J., and Johnson, S. E.: Modification of crustal seismic anisotropy by geological](#)
1205 [structures \(“structural geometric anisotropy”\). Geosphere, 15, 1, 146-170, 2019.](#)

1206

1207 Olliot, E., Goncalves, P., and Marquer, D.: Role of plagioclase and reaction softening in a metagranite shear
1208 zone at mid-crustal conditions (Gotthard Massif, Swiss Central Alps), J. metamorphic Geol., 28, 849-871,
1209 2010.

1210

1211 Park, M., and Jung H.: Analysis of electron backscattered diffraction (EBSD) mapping of geological
1212 materials: precautions for reliably collecting and interpreting data on petro-fabric and seismic anisotropy,
1213 Geoscience Journal, DOI: 10.1007/s12303-020-0002-2, 2020.
1214
1215 [Petrescu, L., Pondrelli, S., Salimbeni, S., Faccenda, M., and Group, A. W.: Mantle flow below the central
1216 and greater Alpine region: insights from SKS anisotropy analysis at AlpArray and permanent stations, *Solid
1217 Earth*, 11, 4, 1275–1290, 2020.](#)
1218
1219 Pfiffner, O.A., Frei, W., Finckh, P., and Valasek, P.: Deep seismic reflection profiling in the Swiss Alps:
1220 Explosion seismology results for line NFP 20-EAST, *Geology*, 16, 987-990, 1988.
1221
1222 Pleuger, J., Hundenborn, R. Kremer, K. Babinka, S. Kurz, W. Jansen, E. and Froitzheim, N.: Structural
1223 evolution of Adula nappe, Misox zone, and Tambo nappe in the San Bernardino area: Constraints for the
1224 exhumation of the Adula eclogites. *Mitteilungen der Österreichischen Geologischen Gesellschaft*, 94, 99–
1225 122, 2003.
1226
1227 Pros, Z., Lokajíček, T., Příkryl, R., and Klima, K.: Direct measurement of 3D elastic anisotropy on rocks from
1228 the Ivrea Zone (Southern Alps, NW Italy), *Tectonophysics* 370, 31–47, 2003.
1229
1230 [Puelles, P., Ábalos, B., Gil Ibarguchi, J.I., Rodríguez, J.: Scales of deformation partitioning during
1231 exhumation in a continental subduction channel: A petrofabric study of eclogites and gneisses from NW
1232 Spain. *Journal of Metamorphic Geology*, 36\(2\), 225-254, 2018.](#)
1233
1234 Punturo, R., Kern, H., Cirrincione, R., Mazzoleni, P., and Pezzino, A.: P- and S-wave velocities and densities
1235 in silicate and calcite rocks from the Peloritani mountains, Sicily (Italy): the effect of pressure, temperature
1236 and the direction of wave propagation, *Tectonophysics* 409, 55–72, 2005.
1237
1238 [Qorbani, E., Bianchi, I., and Bokelmann, G.: Slab detachment under the Eastern Alps seen by seismic
1239 anisotropy, *Earth and Planetary Science Letters*, 409, 1, 96–108, 2015.](#)
1240
1241 Reuss A. Berechnung der Fließgrenze von Mischkristallen auf Grund der Plastizitätsbedingung für
1242 Einkristalle, *Z Angewandte Mathematik Mechanik*, 9, 49-58, 1929.
1243
1244 [Sandmann, S., Nagel, T. J., Herwartz, D., Fonseca, R. O. C., Kurzański, R. M. and Münker, C.: Lu–Hf garnet
1245 systematics of a polymetamorphic basement unit: new evidence for coherent exhumation of the Adula
1246 Nappe \(Central Alps\) from eclogite-facies conditions. *Contributions to Mineralogy and Petrology*, 168, 1–
1247 21, 2014.](#)
1248
1249 Sayers, C.: Long-wave seismic anisotropy of heterogeneous reservoirs, *Geophys. J. Int.*, 132, 667-673.
1250
1251 Schaltegger, U.: Unravelling the pre-Mesozoic history of Aar and Gotthard massifs (Central Alps) by isotopic
1252 dating – a review, *Schweiz. Mineral. Petrogr. Mitt.*, 74, 41-51, 1994.

1253
1254 Schmid, S. M., Fügenschuh, B., Kissling, E., and Schuster, R.: Tectonic map and overall architecture of the
1255 Alpine orogeny, *Eclogae Geologicae Helvetiae*, 97, 93–117, 2004.
1256
1257 Schmid, S. M., and E. Kissling: The arc of the western Alps in the light of geophysical data on deep crustal
1258 structure, *Tectonics*, 19, 1, 62–85, 2000.
1259
1260 Schmidtke, M. J., Keppler, R., Kossak-Glowczewski, J., Froitzheim, N., and Stipp, M.: Elastic anisotropies of
1261 rocks in a subduction and exhumation setting, *Solid Earth*, [submitted 2021](#).
1262
1263 Silver, P.G.: Seismic anisotropy beneath the continents: probing the depths of geology. *Annual Review*,
1264 *Earth and Space Science*, 24, 385, 1996.
1265
1266 Simancas, J. F., Tahiri, A., Azor, A., González Lodeiro, F. Martínez Poyatos, D., and El Hadi, H.: The tectonic
1267 frame of the Variscan-Alleghanian Orogen in Southern Europe and Northern Africa, *Tectonophysics*, 398,
1268 181–198, 2005.
1269
1270 Smith, G.P. and Ekström, G.: A global study of Pn anisotropy beneath continents, *Journal of geophysical*
1271 *Research*, 104, 963–980, 1999.
1272
1273 Steck, A.: Une carte des zones de cisaillement ductile des Alpes Central, *Eclogae Geologicae Helvetiae*, 83,
1274 3, 603-627, 1990.
1275
1276 [Stipp, M. and Kunze, K.: Dynamic recrystallization near the brittle-plastic transition in naturally and](#)
1277 [experimentally deformed quartz aggregates. – *Tectonophysics* 448, 77-97, TECTO124034,](#)
1278 [10.1016/j.tecto.2007.11.041, 2008.](#)
1279
1280 [Stünitz, H., Thust, A., Heilbronner, R., Behrens, H., Kilian, R., Tarantola, A. and Fitz Gerald, J.D.: Water](#)
1281 [redistribution in experimentally deformed natural milky quartz single crystals - Implications for H2O](#)
1282 [weakening processes. *Journal of Geophysical Research, Solid Earth*, 122, 866-894, 2017.](#)
1283
1284 Ullemeyer, K., Leiss, B., and Stipp, M.: Textures and Microstructures in Peridotites from the Finero Complex
1285 (Ivrea Zone, Alps) and its Influence on the Elastic Rock Properties, *Solid State Phenomena* 160, 183-188,
1286 2010.
1287
1288 Ullemeyer, K., Lokajíček, T., Vasin, R.N., Keppler, R., and Behrmann, J.H.: Extrapolation of bulk rock elastic
1289 moduli of different rock types to high pressure conditions and comparison with texture-derived elastic
1290 moduli, *Phys. Earth Planet. Inter.*, 275, 32-43, 2018.
1291
1292 Ullemeyer, K., Siegesmund, S., Rasolofosaon, P.N.J., and Behrmann, J.H.: Experimental and texture-derived
1293 P-wave anisotropy of principal rocks from the TRANSALP traverse: an aid for the interpretation of seismic
1294 field data, *Tectonophysics* 414, 97–116, 2006.

1295
1296 Ullemeyer, K., Spalthoff, P., Heinitz, J., Isakov, N. N., Nikitin, A. N., and Weber, K.: The SKAT texture
1297 diffractometer at the pulsed reactor IBR-2 at Dubna: Experimental layout and first measurements. Nuclear
1298 Instruments and Methods of Physical Research, 412, 80–88, 1998.
1299
1300 Vasin, R., Wenk, H.-R., Kanitpanyacharoen, W., Matthies, S., and Wirth, R.: Anisotropy of Kimmeridge
1301 shale, J. Geophys. Res. Solid Earth, 118, 3931–3956, 2013.
1302
1303 Vasin, R.N., Lebensohn, R.A., Matthies, S., Tome, C.N., and Wenk, H.-R.: The influence of grain shape and
1304 volume fraction of sheet silicates on elastic properties of aggregates: biotite platelets in an isotropic
1305 matrix, Geophysics, 79, 433–441, 2014.

1306 Vasin, R.N., Kern, H., Lokajíek, T., Svitek, T., Lehmann, E., Mannes, D.C., Chaouche, M., and Wenk, H.-R.:
1307 Elastic anisotropy of Tambo gneiss from Promontogno, Switzerland: a comparison of crystal orientation
1308 and microstructure-based modelling and experimental measurements, Geophys. J. Int., 209, 1–20, 2017.

1309 Vaughan, M.T., and Guggenheim, S.: Elasticity of muscovite and its relationship to crystal structure, J.
1310 Geophys. Res. 91, 4657–4664, 1986.
1311
1312 Vernik, L.: Seismic petrophysics in quantitative interpretation. Society of Exploration Geophysicists, DOI:
1313 10.1190/1.9781560803256, 2016.
1314
1315 Vilhelm, J., Rudajev, V., Zivor, R., Lokajíek, T., and Pros, Z.: Influence of crack distribution of rocks on P-
1316 wave velocity anisotropy – a laboratory and field scale study, Geophysical Prospecting 58, 1099-1110,
1317 2010.
1318
1319

1320 Voigt W. Theoretische Studien über die Elasticitätsverhältnisse der Krystalle. Dieterichsche Verlags-
1321 Buchhandlung, Göttingen. 1887. 100 pp.
1322
1323 [Vollbrecht, A., S. Rust, K. Weber: Development of microcracks in granites during cooling and uplift:
1324 examples from the Variscan basement in NE-Bavaria \(FRG\). J. Struct. Geol. 13, 787-799, 1991.](#)
1325
1326 [Vollbrecht, A., H. Dürrast, J. Kraus, K. Weber: Paleostress directions deduced from microcrack fabrics in
1327 KTB core samples and granites from the surrounding area. Sci. Drill. 4, 233-241, 1994.](#)
1328
1329 [Vollbrecht, A., Stipp, M. and Olesen, N. Ø.: Crystallographic orientation of microcracks in quartz and
1330 inferred deformation processes: a study on gneisses from the German Continental Deep Drilling Project
1331 \(KTB\). Tectonophysics 303, 279-297, 1999.](#)
1332
1333

1334 Von Dreele, R.B.: Quantitative texture analysis by rietveld refinement, *J. Appl. Cryst.* 30, 517–525, 1997.
1335
1336 Walsh, J.B.: The effect of cracks on the compressibility of rock. *Journal of Geophysical Research*, 70(2),
1337 381-389, 1965.
1338
1339 Wehrens, P., Baumberger, R., Berger, A., and Herwegh, M.: How is strain localized in a meta-granitoid,
1340 mid-crustal basement section? Spatial distribution of deformation in the central Aar massif (Switzerland),
1341 *Journal of Structural Geology*. 94. 10.1016/j.jsg.2016.11.004, 2016.
1342
1343 Weiss, T., Siegesmund, S., Rabbel, W., Bohlen, T., and Pohl, M.: Seismic Velocities and Anisotropy of the
1344 Lower Continental Crust: A Review, *Pure appl. geophys.*, 156, 97–122, 1999.
1345
1346 Wenk, H.-R., Lutterotti, L., and Vogel, S.C.: Rietveld texture analysis from TOF neutron diffraction data,
1347 *Powder Diffraction* 25, 283–296, 2010.
1348
1349 [Wenk, H.-R., Matthies, S., Donovan, J., Chateignier, D: BEARTEX, a Windows-based program system for](#)
1350 [quantitative texture analysis. *J. Appl. Cryst.* 31, 262–269, 1998.](#)
1351
1352 Wenk, H.-R., Yu, R., Vogel, S., and Vasin R. Preferred orientation of quartz in metamorphic rocks from the
1353 Bergell Alps, *Minerals* 9(5), 277, 2019.
1354
1355 Worthington, J.R., Hacker, B.R., and Zandt, G.: Distinguishing eclogite from peridotite: EBSD-based
1356 calculations of seismic velocities. *Geophys. J. Int. Seism.* DOI:10.1093/gji/ggt004, 2013
1357
1358 Yan, Z., R. W. Clayton, and J. Saleeby: Seismic refraction evidence for steep faults cutting highly attenuated
1359 continental basement in the central transverse ranges, California, *Geophys. J. Int.*, 160, 651–666, 2005.
1360
1361 Zappone, A., Fernández, M., García-Duenas, V., and Burlini, L.: Laboratory measurements of seismic P-wave
1362 velocities on rocks from the Betic chain (southern Iberian Peninsula), *Tectonophysics* 317, 259–272, 2000.
1363
1364 Zel, I.Yu., Ivankina, T.I., Levin, D.M., Lokajicek, T.: P-wave ray velocities and the inverse acoustic problem
1365 for anisotropic media. *Crystallography Reports* 61, 4, 623-629, 2016.
1366
1367 Zertani, S., John, T., Tilmann, F., Motra, H. B., Keppler, R., Andersen, T. B., and Labrousse, L.: Modification
1368 of the seismic properties of subducting continental crust by eclogitization and deformation processes.
1369 *Journal of Geophysical Research: Solid Earth*. 124, 9731-9754, 2019.
1370
1371 Zertani, S., Vrijmoed, J. C., Tilmann, F., John, T., Andersen, T. B., and Labrousse, L.: P wave anisotropy
1372 caused by partial eclogitization of descending crust demonstrated by modeling effective petrophysical
1373 properties. *Geochemistry, Geophysics, Geosystems*. 20, DOI: 10.1029/2019GC008906, 2020.
1374

- 1375 Zhang J.J., Santosh M., Wang X.X., Guo L., Yang X.G., and Zhang B.: Tectonics of the northern Himalaya
1376 since the India–Asia collision, *Gondwana Research*, 21, 4, 939–960, 2012.
1377
1378 Zhang, J.F., Wang, Y.F., and Jin, Z.M.: CPO-induced seismic anisotropy in UHP eclogites, *Sci China Ser D-*
1379 *Earth Sci*, Vol. 51, No. 1, 11-21, 2008.
1380